Geoderma 440 (2023) 116721

Contents lists available at ScienceDirect

Geoderma

journal homepage: www.elsevier.com/locate/geoderma

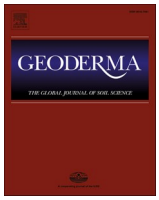

Three-dimensional X-ray imaging of macropore flow

Anna Elena Schwenk [a], Nicholas Jarvis [a], Mats Larsbo [a], John Koestel [a,b,*]

[a] Department of Soil and Environment, Swedish University of Agricultural Sciences (SLU), P.O. Box 7014, 750 07 Uppsala, Sweden
[b] Soil Quality and Soil Use, Agroscope, Reckenholzstrasse 191, 8046 Zürich, Switzerland

ARTICLE INFO

Handling Editor: Y. Capowiez

Keywords:
X-ray imaging
Macropore flow
Kinematic wave equation
Kozeny equation
Soil physics
Preferential flow
Air entrapment

ABSTRACT

Macropores are known to be important pathways for the rapid transport of water, solutes and colloids in soil. Nevertheless, we still know very little about how the topology and geometry of macropore networks govern water flow configurations and velocities in natural soil. In this study, we aimed at gaining more insight into macropore flow by using X-ray tomography to quantify air–water distributions in the macropore networks of undisturbed topsoil and subsoil columns of a clay soil at varying steady-state flow rates. We observed that while large fractions of the macropore network remained air-filled, the air phase only became entrapped when the irrigation rate was very close to the saturated hydraulic conductivity of the soil. The data enabled us to parameterize a kinematic wave model for water flow following the approach proposed in Jarvis et al. (2017a). Follow-up experiments would be required to evaluate whether these kinematic wave parameters derived by X-ray imaging match with those obtained from outflow measurements. We found that quantitative X-ray imaging of macropore flow through soils still remains a challenging task. We recommend that future experiments are conducted on smaller soil samples to improve image resolution and minimize experimental time spans as well as X-ray image noise and illumination bias. Such experiments could also include 3-D tracer imaging to identify the imaged macropore networks transporting most of the water (i.e. the backbone) at varying steady irrigation rates.

1. Introduction

During rainfall, a large proportion of the water recharging through the unsaturated zone may be channeled at high velocities through large structural macropores (e.g. root or earthworm channels, inter-aggregate pore space, fissures) that represent "paths of least resistance" in soil (Beven and Germann, 1982; Nimmo, 2021). Macropores have important beneficial impacts on the hydrological cycle, since they enhance infiltration capacity and drainage rates, thereby minimizing the risks of waterlogging, surface runoff, soil erosion and flooding (Beven and Germann, 1982). On the other hand, the rapid 'non-equilibrium' flow of water through soil macropores is also associated with significant ecosystem disservice, since it can dramatically accelerate the leaching of contaminants to surface water and groundwater (Jarvis, 2007).

The strength of preferential flow is controlled by boundary conditions (i.e. rainfall or irrigation intensities (e.g. Demand et al., 2019; Gao et al., 2018; Hincapié and Germann, 2009; Jarvis, 2007) in relation to the properties of the soil pore network, especially pore size (diameter) distribution and connectivity (Katuwal et al., 2015; Larsbo et al., 2014). The application of X-ray CT technologies has shown that soil macroporosity is comprised of one or more pore networks (clusters), each characterized by multiple pathways of variable thickness, including bottleneck constrictions and 'dead-end' or dangling pores (e.g. Luo et al., 2010; Perret et al., 1999; Pierret et al., 2002). It has been suggested that concepts derived from percolation theory should prove useful to describe the connectivity of macropore networks (Jarvis et al., 2017b; Larsbo et al., 2014; Soto-Gómez et al., 2020). Within this theoretical framework, macroporosity is either isolated or comprises part of the 'percolating network' (i.e. pore space that forms a connected cluster across the sample). The 'percolating porosity' comprises a 'backbone' fraction (i.e. that part in which water would predominantly flow through the sample under saturated conditions) as well as dead-end pores (that part with stagnant water at saturation; (Hunt et al., 2014)). These three pore categories (isolated, backbone and dead-end) correspond to the terms remote, arterial and marginal pores used in an earlier classification system underlying a model of gas diffusion in soil (Arah and Ball, 1994; Lamandé et al., 2021). Very little is known about how initial and boundary conditions interact with the topology and geometry of macropore networks to govern water flow configurations and velocities in natural soils (Nimmo, 2021). In this respect, the

* Corresponding author at: Department of Soil and Environment, Swedish University of Agricultural Sciences (SLU), P.O. Box 7014, 750 07 Uppsala, Sweden.
E-mail address: john.koestel@slu.se (J. Koestel).

https://doi.org/10.1016/j.geoderma.2023.116721
Received 26 May 2023; Received in revised form 20 September 2023; Accepted 18 November 2023
Available online 3 December 2023

influence of the air phase on water flow in soil macropores during infiltration (Carrick et al., 2011; Culligan et al., 2000) is generally overlooked even though the significance of air entrapment and release was recognized more than 50 years ago (Dixon and Peterson, 1971; Dixon and Linden, 1972).

The importance of macropore flow has prompted the development of many models of varying complexity and conceptual basis that can account for the effects of macropores on water flow and solute transport (Jarvis et al., 2016). These models can function as useful tools for testing and developing our understanding of the process and for making predictions. The most mechanistic modelling approaches rely on advances in X-ray tomography and numerical computational methods that enable applications of the fundamental Navier-Stokes equations for viscous fluid flow to imaged pore networks (e.g. Dal Ferro et al., 2015; Gackiewicz et al., 2022; Scheibe et al., 2015). In principle, modelling flow directly at the pore-scale allows the impacts of macropore flow at much larger scales (e.g. a soil profile) to emerge as a consequence of the characteristics of the macropore network and the imposed boundary conditions. However, because of technical constraints on spatial and temporal scales imposed by both X-ray scanning and the computational methods, simpler models are more widely employed (Jarvis et al., 2016). Analytical solutions of the Navier-Stokes equations for idealized flow geometries, such as free water films of constant width or fully saturated flow through slits or cylindrical pores (i.e. the Hagen-Poiseuille equation) may provide some insights into the factors controlling preferential flow (e.g. Demand and Weiler, 2021). For example, for the same input rate and all other things being equal, this theory suggests that laminar water flow in thin films along macropore walls should be four times faster than flow in saturated fissures of the same width. However, the usefulness of these simple analytical solutions is limited to some extent by the assumption of steady-state and the idealized representation of the flow geometry, as the configuration of water flowing in macropores will change under transient conditions (Jarvis, 2007).

Jarvis et al., (2017a) showed how the kinematic wave equation for macropore flow, which was originally proposed by Germann (1985), can encompass these analytical solutions of the Navier-Stokes equations as special cases in a generalized physics-based model. This macroscopic approach assumes that a power law relationship exists between the wetted surface area and water saturation in an "equivalent" flow pathway (Jarvis et al., 2017a). In this model, the exponent in the power law, given by (3-α)/2 where α is the well-known kinematic exponent (Germann, 1985), controls the flow configuration and thus the macropore water velocity for any given input rate. Combining the kinematic wave equation with an equation of continuity enables the simulation of water flow in a macropore network under transient conditions. A kinematic wave can also be combined with standard descriptions of water flow and solute transport in the soil matrix in a dual-permeability framework (Larsbo et al., 2005) to significantly enhance the potential range of applications of the model.

Most applications of the kinematic wave equation so far have relied on calibration of model parameters against measured data on water flow (Jarvis and Larsbo, 2012), mostly because methods to directly measure them have been lacking. This makes it difficult to critically test the underlying model concepts and raises the question of whether or not the model is matching the data for the right reasons. X-ray scanning to quantify water in soil macropores directly in connection with flow experiments (Heijs et al., 1995; Koestel and Larsbo, 2014; Mooney, 2002; Sammartino et al., 2012; Sammartino et al., 2015) may help to resolve this issue. In particular, the advent in recent years of advanced image analysis algorithms to quantify the volumes and spatial arrangement of solids, water and air phases in soil (Helliwell et al., 2013; Schlüter et al., 2014) may allow direct tests of the assumptions underlying the kinematic wave equation. For example, Lissy et al. (2020) recently made use of data of X-ray imaged soil macropore networks to parameterize a 1-D dual-domain model that employed the kinematic wave equation for water flow in macropores. They concluded that at least some of the model parameters could be derived from soil structural features, more specifically the effective macroporosity and the average macropore separation. The main overall objective of our study was to gain a better understanding of water flow in macropores by utilizing X-ray tomography to quantify flow configurations (i.e. air–water distributions) in the macropore networks of undisturbed topsoil and subsoil columns of a clay soil at varying steady-state flow rates. Another and more specific objective was to use this image data to test a key assumption underlying the kinematic wave equation, namely that a power law relationship exists between the degree of saturation and the wetted surface area in macropores (Jarvis et al., 2017a).

Table 1
Texture and organic carbon contents of the investigated soil.

	Sand (g/g)	Silt (g/g)	Clay (g/g)	SOC (g kg^{-1})
Topsoil	0.29	0.30	0.41	13.6
Subsoil	0.16	0.22	0.62	10

2. Materials and methods

2.1. Soils and sites

Four intact cylindrical soil samples (inner diameter 91 mm, height approximately 100 mm) were excavated from a conventionally-tilled arable field near Ultuna, Sweden (59° 49′ N 17° 39′ E) on 28th September 2017, after harvest of the preceding cereal crop, but before autumn cultivation. The samples were obtained by slowly and carefully pushing hollow aluminum cylinders (wall thickness 4.55 mm, height 110 mm) into the ground with a hydraulic press that was temporarily installed and anchored at the site. We attached ring-shaped stainless steel blades to the aluminum cylinders to facilitate insertion. We took care to collect the samples such that their upper surface was 1 cm below the upper end of the aluminum cylinders. Two samples each from the topsoil (0 to 10 cm depth) and the subsoil (30 to 40 cm depth) were retrieved. In the following, we refer to the topsoil and subsoil samples as T1 and T2 and S1 and S2, respectively. Texture and soil organic carbon contents of the topsoil and subsoil are summarized in Table 1. The bottom of each sample was carefully trimmed and a nylon cloth was applied. The columns were placed in a water bath and slowly wetted from the bottom until water was observed at the soil surface. Subsequently, they were placed on a sand bed, with a matric potential of −30 cm applied at the bottom surface until drainage out of the soil samples ceased. This matric potential was chosen because we wanted all pores below the X-ray image resolution to remain saturated with water. Assuming perfect wettability, the Young-Laplace equation predicts that pores of diameter smaller than 100 μm, corresponding approximately to the voxel edge length, would be saturated. The samples were then placed in air-tight plastic bags and stored in a cold room at 4 °C until the start of the irrigation experiments.

2.2. Irrigation device

We used self-designed irrigation heads connected to piston pumps (*Prominent Dosingpump Gamma/X*) to irrigate the soil samples inside the *GE Phoenix v|tome|x 240 m* X-ray scanner located at the Department of Soil and Environment at the Swedish University of Agricultural Sciences in Uppsala, Sweden. The irrigation heads were mounted on a rail system that had been welded to the ceiling of the X-ray hatch. The rail system allowed flexible positioning of the irrigation head in all three directions of space. Each irrigation head was manufactured out of Plexiglas. It had an outer diameter of 100 mm and included a small water reservoir with a diameter of 75 mm and 20 mm height. At the bottom of the reservoir, the water was channeled to 16 dental cannulas (inner diameter 0.4 mm) that

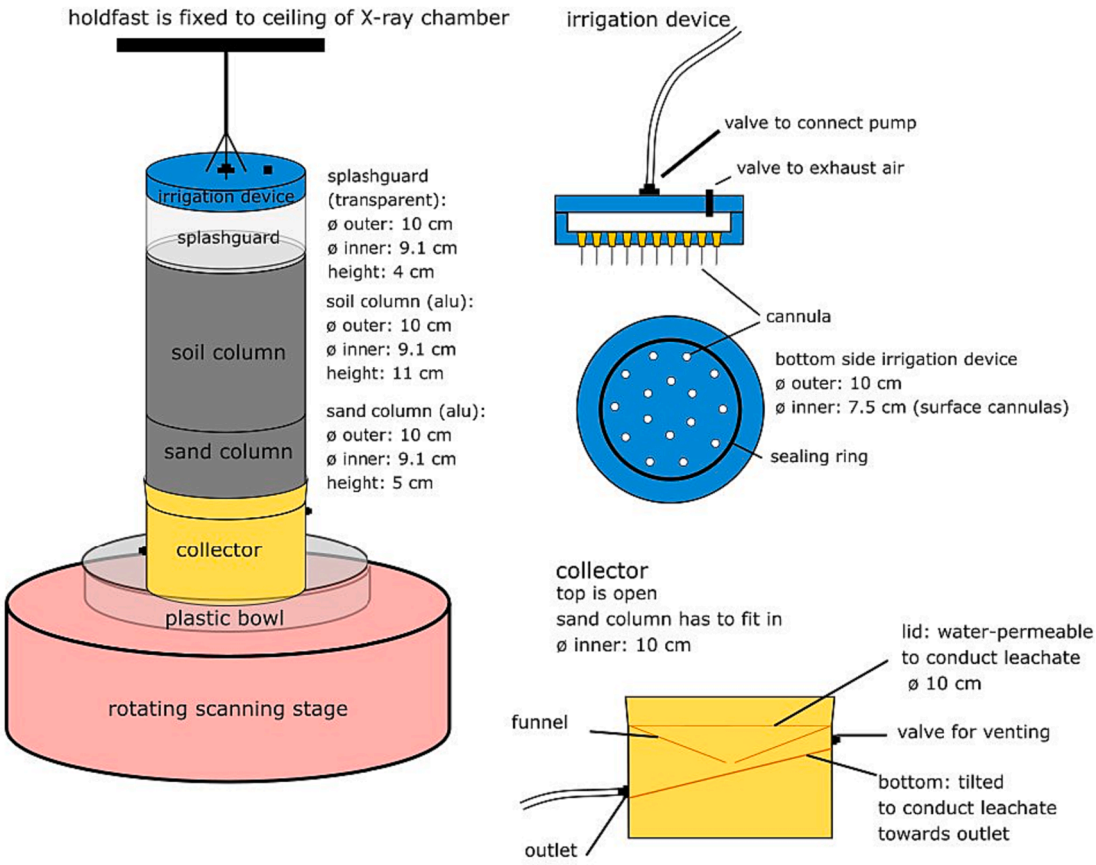

Fig. 1. Schematic illustration of the design of irrigation heads, effluent collector and experimental setup.

were arranged approximately equidistantly. A lockable opening was installed at the top of the irrigation head for venting. A hose for water supply was attached at the top of the reservoir and connected with a piston pump, which in turn was connected to a larger reservoir filled with artificial rainwater (Löv et al., 2017), which was placed inside the X-ray scanner on the floor. Fig. 1 illustrates the design of the irrigation head. Prior to the experiments, we carefully tested and calibrated the irrigation heads. The setup provided approximately uniform irrigation rates between 1 and 50 mm h^{-1}.

2.3. Experimental set-up

The soil samples were mounted on a 50 mm tall column filled with fine sand, which was in turn placed on a 3-D printed funnel system and a scale on a large plastic tray. The sand column was included to avoid saturation at the bottom of the soil sample. Both the sand column and the funnel had the same diameter as the aluminum cylinder containing the soil sample. Nylon cloths were installed at the bottom of the sand column to keep the sand in place. The scale was used to keep track of the water content changes inside the column to check when steady-state flow conditions had been established. The effluent water was conducted through a tube to a small tank. The tray collected occasional water drops. A metal grating was mounted on top of the soil column to reduce the risk of splash erosion during irrigation. Fig. 1 illustrates the design of the funnel system and the experimental set-up inside the X-ray scanner.

2.4. Experimental schedule

Prior to each irrigation experiment, the soil column was scanned by X-ray after it had been drained to a matric potential of −30 cm. The soil sample was then irrigated inside the scanner at a rate of 2 mm h^{-1} until steady-state conditions had established. This was assumed once there was no measurable increase in column weight during one hour. Upon reaching steady-state, another X-ray image was taken, whereupon the irrigation rate was increased to 5 mm h^{-1}. This sequence was continued at larger irrigation rates until the sample showed signs of ponding. We were able to record 3-D images of both topsoil samples at irrigation rates of 2, 5, 10 and 50 mm h^{-1}. The final irrigation rate was close to the saturated hydraulic conductivity (K_s) for column T2 as it was starting to pond during the final scan. Column T1 never ponded, so K_s was $>$ 50 mm h^{-1}. The first subsoil sample (S1) ponded at 5 mm h^{-1}. We therefore started the irrigation for the S2 column at 1 mm h^{-1} to image more steady-state irrigation rates. However, the S2 sample ponded already at this lower irrigation rate. Table 2 gives an overview of the 3-D images collected under initial and steady-state conditions.

Table 2
Overview on X-ray images acquired for the investigated soil samples under different irrigation rates.

	Col1	Col4	Col7	Col8
I (mm h^{-1})	T1	T2	S1	S2
0	×	×	×	×
1				×
2	×	×	×	
5	×	×	×	
10	×	×		
50	×	×		

2.5. X-ray imaging

2.5.1. Image acquisition

3-D X-ray images of the four soil samples were obtained prior to the irrigation experiments and also after steady-state conditions had

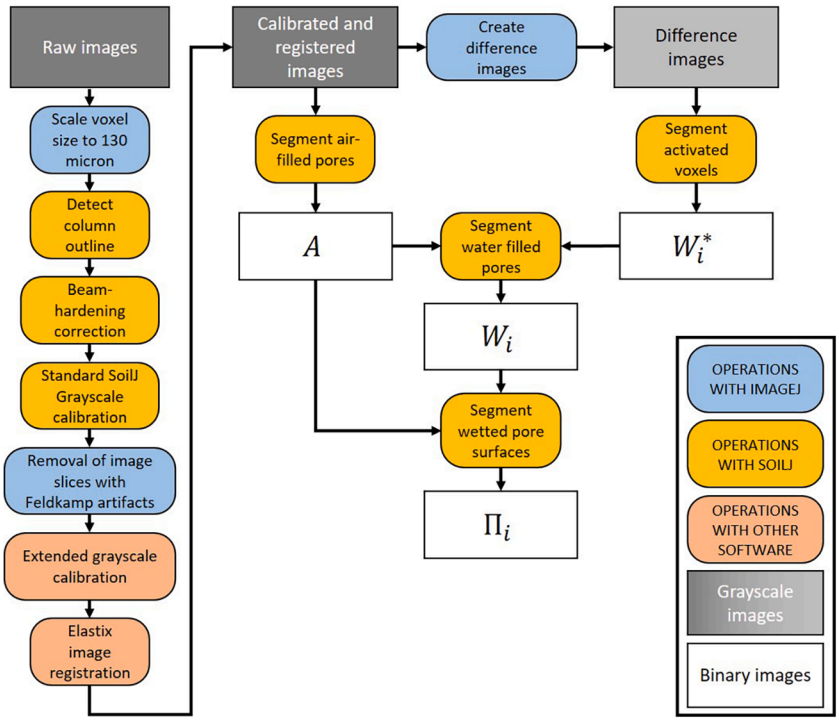

Fig. 2. Illustration of the image processing and evaluation workflow used in this study.

established at each irrigation rate.

We set the tube voltage to between 130 and 150 kV with an electron flow of 300 to 590 μA and an exposure time of 500 ms or 1000 ms per projection, depending on the bulk density and water content of the sample. We filtered the X-ray beam with 0.5 to 0.9 mm thick copper sheets to reduce beam-hardening artifacts. We collected 2000 projections from equidistant angles along a 360-degree rotation. For each projection, four radiographs were acquired, but the average of only the last three were saved on disk to minimize impacts of detector after-glow. These settings gave an acquisition time of 66 min per 3-D image. The voxel size was 65 μm. The projections were reconstructed to 3-D images using the GE Phoenix software *datos* version 2.1.0.582.

2.5.2. *Image preparation*

All X-ray images were pre-processed with SoilJ (Koestel, 2018), a plugin for the open imaging software ImageJ/FIJI (Schindelin et al., 2012; Schneider et al., 2012). We used the workflow outlined in Fig. 2. First, the image voxel edge length was scaled to 130 μm (corresponding to an image resolution of 2- to 3- times the voxel edge length, i.e. approximately 330 μm) to reduce the calculation time required for the following image processing steps. The columns were then moved to an upright position in the center of the image and unused canvas was removed to decrease the image file size. The outlines of the column walls were detected and saved. Beam-hardening artefacts were reduced using the algorithm implemented in the SoilJ software (Koestel, 2018). The gray-scale of each horizontal image cross-section was calibrated using the standard approach in the SoilJ workflow. In short, gray-scale values corresponding to air (estimated by the 0.1 percentile of the gray-values within the horizontal-cross-section) and the aluminium column wall served as references. The image gray-scales were then linearly scaled for all image voxels such that air and the aluminium column wall had gray-values of 5,000 and 20,000, respectively:

$$\gamma_{x,y,z} = \frac{k_{x,y,z} - k_{air,z}}{k_{alu,z} - k_{air,z}} 15,000 + 5,000 \quad (1)$$

where $\gamma_{x,y,z}$ (-) and $k_{x,y,z}$ (-) are the calibrated and uncalibrated gray-values at coordinates x, y, z (mm), respectively, and $k_{air,z}$ and $k_{alu,z}$ are the uncalibrated estimates of the gray-values corresponding to air and aluminium in depth z, respectively. In this fashion, larger illumination artifacts, which often occur for industrial X-ray scanners in the vertical direction, were corrected.

Gray-values in the calibrated images of less than 8,000 represented air-filled imaged macropores (see Fig. A1). A closer inspection of the calibrated gray-values below this threshold revealed that they i) were depth dependent (Fig. A2), ii) became non-linearly larger with distance from the column walls (Fig. A3) and iii) depended on the irrigation rates (Figs. A2 & A3). In addition, regions with calibrated gray-values >16,000 and ≤20,000, corresponding to dense soil matrix and lighter gravel and sand grains, became smaller with increasing irrigation rate. Radial bias in this image phase was also present. These image illumination heterogeneities resulted in poor mass balances (see Fig. A4 as an example). There were no indications that the gray-value drift was caused by incomplete saturation of the soil matrix at the beginning of the experiment. Instead, we strongly suspect that the drift in illumination with irrigation rate was caused by X-ray scattering on water molecules: the scattering artifacts became more pronounced with increased soil water contents. We therefore developed an extended gray-scale calibration (see Fig. 2).

The extended gray-scale calibration consisted of three consecutive steps: i) correction of residual gray-scale fluctuations in the vertical direction, ii) correction of radial gray-scale fluctuations, iii) masking of gray-values below or above the gray-value range of interest. Before applying the first step, we trimmed the X-ray images as follows. We considered regions of interest (ROI) corresponding to the entire horizontal cross-section of each soil sample and sample heights of between 78 and 84.5 mm. The top and bottom of the ROI were defined by the first and last horizontal slices that were unaffected by Feldkamp artefacts.

To correct the residual vertical gray-value fluctuations, we sampled all image voxels that had gray values smaller than 8,000 (i.e. air-filled pores) in all recorded images (i.e. the initial state and all irrigation rates under steady flow). Next, we sampled all voxels with gray values between 15,000 and 17,000 in all images (see Fig. A1). These voxels represent the dense soil matrix, which we assumed to be fully water saturated prior to the first irrigation and, hence, to exhibit a constant

bulk density throughout the experiment. We then corrected for gray-value fluctuations in the vertical direction, using

$$\gamma'_{x,y,z} = \frac{\gamma_{x,y,z} - \gamma_{air,z}}{\gamma_{dmp,z} - \gamma_{air,z}} \left(\gamma^{0}_{dmp,z} - 5000\right) + 5000 \quad (2)$$

where $\gamma'_{x,y,z}$ (-) and $\gamma_{x,y,z}$ (-) are the corrected and uncorrected gray-values at coordinates x, y, z (mm), $\gamma_{dmp,z}$ (-) and $\gamma_{air,z}$(-) are the average gray-values of the dense matrix and the air-phase at depth z, respectively, and $\gamma^{0}_{dmp,z}$ (-) is the average gray-value of the corresponding depth in the image collected prior to the irrigations.

To eliminate radial gray-value drifts, we used equation (3):

$$\gamma''_{x,y,z} = \frac{\gamma'_{x,y,z} - \gamma'_{air,r}}{\gamma'_{dmp,r} - \gamma'_{air,r}} \left(\gamma^{0'}_{dmp,r} - 5000\right) + 5000 \quad (3)$$

where $\gamma''_{x,y,z}$ is the final corrected gray-value at location x, y and z, $\gamma'_{dmp,r}$ and $\gamma'_{air,r}$ are average gray-values (averaged over all depths) at the radial distance r (mm) from the central vertical axis of the soil sample. The superscript $0'$ denotes again gray-values of the image collected prior to the irrigation.

These illumination correction steps only corrected for symmetrical gray-scale drifts. Local illumination heterogeneities were still included in the images. For example, some voxels depicting air-filled pores with gray-values of less than 5000 still exhibited changes with irrigation rate, despite all our efforts at correction. Likewise, illumination drifts with irrigation rate could neither be fully corrected for gray-values of the dense matrix phase nor for sand and gravel grains. All these illumination drifts led to artifacts later on in the image analyses workflow, namely when evaluating difference images (see next section and Fig. 2). We therefore set all gray-values <5000 to 5,000 and all gray-values >13,000 to 13,000 (see Fig. A1 for illustration). The latter threshold was found after analyzing the gray-scale of voxels that displayed relevant increases in image brightness with irrigation rate, which was on average the case for voxels with gray values smaller than ca. 13,000 under the highest irrigation rate.

2.5.3. Imaging water content changes

The images collected under steady-state irrigation were aligned to the image collected prior to the onset of irrigation. We used the rigid registration approach implemented in the elastix software (Klein et al., 2010; Shamonin et al., 2014). Four landmarks, whose image coordinates were obtained upon visual inspection, were used to guide the registration for each image pair. After the images were roughly aligned, we applied an elastic registration to correct for local modifications of the pore-space geometry that had occurred with increasing water saturation. We used the BSpline registration in the elastix software. This registration tool minimizes the Mattes mutual information criterion under the constraint of a bending energy penalty, using identical regularization weights for all registrations. A five-step pyramid scheme was used to carry out the elastic registration on ever-finer resolutions.

After the images were registered, we created difference images by subtracting the image obtained prior to the first irrigation from the images of the irrigated columns. Upon visual inspection of the histograms of the difference images, we found that large water-filled pores had gray values of approximately 4,000 (see Fig. A5 for illustration). We then obtained the image derived increase in the mass of water $M_{w(X)}$ (g) in the soil column by summing up the gray-values of all voxels in the ROIs of the difference images, dividing them by 4,000 and multiplying them by the voxel volume and the density of water at 20 °C.

We then segmented the difference images selecting a threshold value of 1,000. This threshold corresponds to the noise level in the images, which means that only a very small number of voxels were "activated" solely due to image noise. However, this does not mean that the chosen threshold will result in a correct segmentation of the visible water phase and we do not have any independent data for verification. On average, all voxels with an increase in gray value corresponding to a water volume increase corresponding to 25 % of the voxel volume are segmented as "activated". Pores with diameters smaller than the actual image resolution would also be captured if they filled with a sufficient amount of water. We referred to such voxels as 'activated' voxels in the following and marked associated variables and images with an asterisk. The segmented difference images are in the following referred to as W_i^*, where the subscript i indicates the irrigation rate.

2.5.4. Segmentation of air-filled macropores

The visible, air-filled pore network was segmented for all collected 3-D images. We averaged the histogram of all 3-D images of each individual sample (e.g. for sample T1 it was five images in total: the image before irrigation together with the images under steady-state irrigation at 2, 5, 10 and 50 mm h^{-1}). We applied the gray-scale threshold of 8,000 to segment the air-filled macropores in all images. In the following, we refer to the binary images of air-filled porosity as A_i where the index indicates the i^{th} irrigation rate with $i = 0$ denoting no irrigation.

2.5.5. Extracting water in X-ray visible pores

As discussed above, the volumes W_i^* for which an increase in water content was detected also included voxels containing pores with diameters below the image resolution. An additional image-processing step was necessary to segment the activated voxels in the image-resolvable pores

$$W_i = W_i^* \wedge A_o \quad (4)$$

where A_0 is the binary image depicting the (air-filled) macropores prior to the onset of irrigation.

2.5.6. Segmenting percolating water and air phases as well as entrapped air

By definition, a percolating water or air cluster is connected to both the top and the bottom surface. We extracted percolating water and air phases for all binary images W_i^*, W_i and A_i by removing all disconnected water or air phase voxels. The resulting images are denoted as $W^*_{i(p)}$, $W_{i(p)}$ and $A_{i(p)}$ in the following. The percolating air phase extracted from the images taken prior to the start of the flow experiments is equivalent to the percolating X-ray visible macroporosity. All air clusters without a connection to the top surface were considered as entrapped air, assuming that air could not escape through the seepage face at the bottom of the sand column on which the sample had been placed.

2.5.7. Calculating morphological properties of imaged water and air phases

We used the ImageJ plugins SoilJ (Koestel, 2018) and MorphoLibJ (Legland et al., 2016) to derive morphological properties from the different imaged phases. The imaged porosity and specific surface area prior to the onset of irrigation are denoted as φ (mm^3 air mm^{-3} soil volume) and σ (mm^2 air phase interface mm^{-3} soil volume) respectively. From the images W_i^*, we defined θ_w^* (mm^3 water mm^{-3} soil volume) as the volume of all activated voxels (voxels with detected water content changes) divided by the total volume. Similarly, the water content of the imaged macropores derived from the images W_i, is denoted as θ_w (mm^3 water mm^{-3} soil volume), while the air content of the imaged macroporosity derived from the A_i images is denoted as θ_a (mm^3 air mm^{-3} soil volume). We also derived specific surface areas for water and air, σ_w^*, σ_w, σ_a (mm^2 phase interface mm^{-3} soil volume), average phase thicknesses d_w^*, d_w, d_a (mm) and the so-called connection probabilities Γ_w^*, Γ_w and Γ_a (dimensionless), defined as the probability that any two water-(or air-) filled voxels belong to the same cluster (*Renard and Allard*, 2013) corresponding to the binary images W_i^*, W_i and A_i, respectively. Finally, we computed volumes, surfaces, thicknesses and connectivities for the images $W^*_{i(p)}$, $W_{i(p)}$ and $A_{i(p)}$, depicting only the percolating water and air

volumes. The results are denoted as $\theta^*_{w(p)}$, $\theta_{w(p)}$, $\theta_{a(p)}$, $\sigma^*_{w(p)}$, $\sigma_{w(p)}$, $\sigma_{a(p)}$, etc. in the following.

While the calculation of porosity as well as water and air contents are straightforward, we used SoilJ, which makes use of the discretized version of the Crofton formula implemented in MorphoLibJ to calculate specific surface areas (Legland et al., 2016). The phase thicknesses were obtained with aid of the maximal inscribable sphere method, using the ImageJ implementation. The connection probabilities were calculated in SoilJ according to

$$\Gamma = \frac{\sum_{i=1}^{N} n_i^2}{\left(\sum_{i=1}^{N} n_i\right)^2} \tag{5}$$

where n_i is the number of voxels contained in the ith pore-cluster and N is the total number of unconnected pore clusters. The connected-cluster labelling was carried out using SoilJ, which in turn employs the algorithm in MorphoLibJ considering 26 nearest neighbors. The connection probability quantifies how well the voxels of a specific image phase are connected to each other. For example, if air-filled pore voxels are considered, Γ takes on a value of one if all air voxels are connected to each other. The more frequent isolated air voxels (or clusters of air voxels) become, the closer Γ approaches to zero.

2.5.8. Quantification of wetted macropore surfaces

We obtained 3-D images of the macropore surfaces by first morphologically eroding the binary image depicting the macropores prior to irrigation using a 3-D structuring element E with a diameter of three voxels:

$$A_0^- = A_o \ominus E \tag{6}$$

Then, we subtracted the eroded image from the original binary image to obtain the image of the macropore surfaces

$$P = A_o - A_0^- \tag{7}$$

This image was then combined by logical AND operators with the cumulative water content increases to yield the image of the wetted macropore surface area

$$\Pi_i = P \wedge W_i^* \tag{8}$$

for each irrigation rate *i*. The wetted specific macropore surface area was computed for each irrigation rate *i* as

$$s_i = \frac{\sum_v \Pi_i}{\sum_v P} \sigma(\mathrm{mm}^{-1}) \tag{9}$$

where the operator Σ_v denotes the number of non-zero voxels contained within an image. We used the wetted macropore surface to calculate the hydraulic radius

$$r_h = \frac{\theta_w}{s}(\mathrm{mm}) \tag{10}$$

where we omitted adding indices *i* for the different irrigation rates for convenience.

2.6. Flow equations

We used our measurements to parameterize a kinematic wave model of water flow through soil macropores. Our starting point is a generalization of analytical solutions of Stokes law for highly idealized geometries, which employs the concept of hydraulic radius (equation (10)), thereby making it a more generally applicable model to calculate water flow through an "equivalent channel" or pathway. This macroscopic model can be expressed as (Berg, 2014)

$$q_‡ = c\,\theta_‡ r_h^2 \tag{11}$$

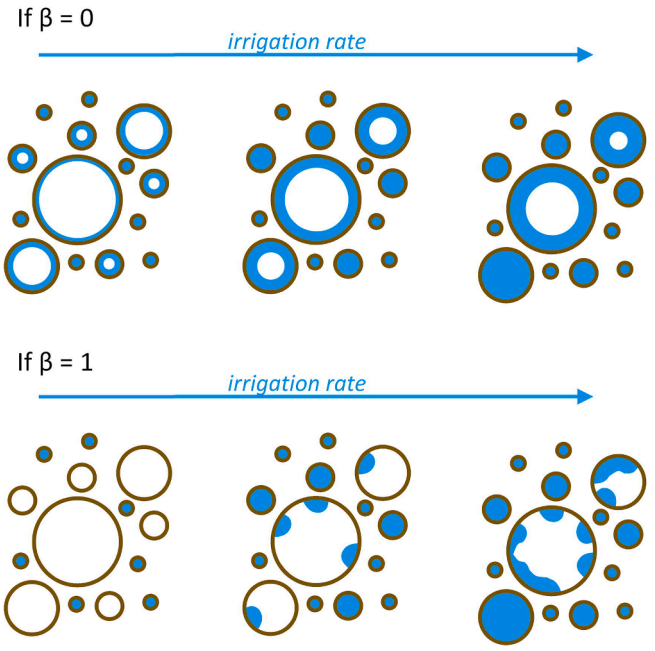

Fig. 3. Schematic illustrating the relationship between wetted macropore surface area and water saturation under different irrigation rates for contrasting values of exponent β (see equation (12).

where $q_‡$ (mm h^{-1}) is the flow rate, $\theta_‡$ (mm^3 mm^{-3}) is the volumetric water content of the equivalent flow pathway and *c* ($mm^{-1}h^{-1}$) is a composite parameter

$$c = \frac{g}{G\mu\tau^2} \tag{12}$$

where *g* (m s^{-2}) is the gravitational acceleration, G (-) is a factor depending on the flow geometry that varies between 2 for cylindrical and 3 for planar geometries (see Childs, 1969; Hoffmann-Riem et al., 1999), μ (m^2 s^{-1}) is the kinematic viscosity and τ (-) is the flow path tortuosity. The temperature in the X-ray scanner is kept constant, so the same will hold for the viscosity μ. The flow geometry G and the tortuosity τ very likely changed to some extent between the different steady-state flow rates. In principle, approximations could be derived from the imaged water-filled macropore network. However, for the sake of simplicity, we assumed here that they also remained constant. For G = 2.5 and a typical value of τ of 2, *c* will take a value of ca. 7 million $mm^{-1}h^{-1}$. The subscripts '‡' in equation (11) denote that these variables in the model may not be identical to the measurements made in our experiments. In particular, we assume that the flow contribution of the sub-resolution pore space in the experiments was negligible, even though it must have carried some of the flow. Data on the near-saturated hydraulic conductivity of Ultuna clay measured by tension infiltrometer in the field (Jarvis and Messing, 1995; Messing and Jarvis, 1993) suggest that this may be a reasonable assumption, except for the smallest flow rates in the columns (i.e. 1–2 mm h^{-1}).

A kinematic wave equation can be derived from equation (11) by assuming that the fractional wetted macropore specific surface area is related to the degree of saturation in the macropores by a power law

$$\frac{s_‡}{\sigma} = \left(\frac{\theta_‡}{\phi}\right)^{\beta} \tag{13}$$

where β (-) can have values between 0 and 1 and reflects the geometrical configuration of water flowing in the macropores and the subscripts '‡' again indicate that the corresponding variables may be distinct from the image-derived measurements explained above. Fig. 3 is a schematic illustration of how the parameter β relates to different macropore flow

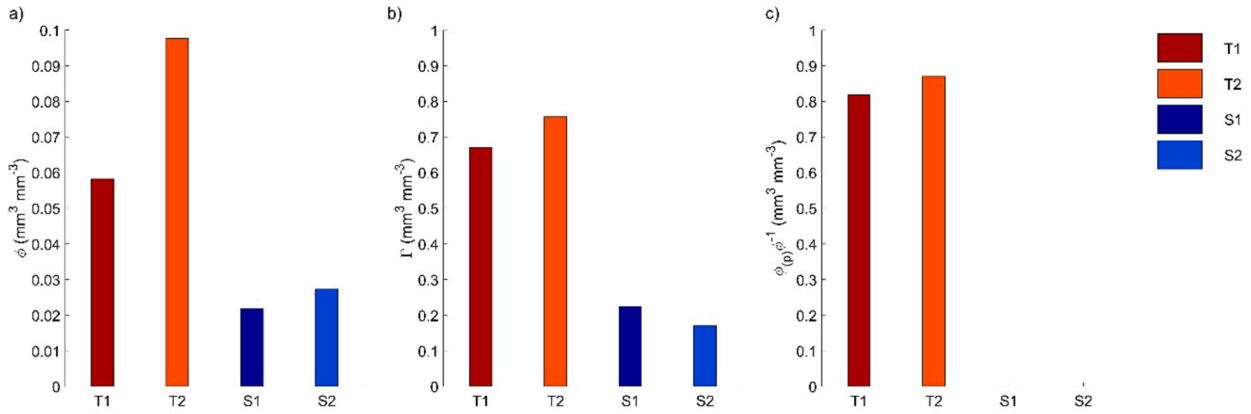

Fig. 4. (a) Imaged macroporosity φ, (b) the connection probability for imaged macroporosity Γ and (c) the fraction of macroporosity that percolates, $\varphi_{(p)}\ \varphi^{-1}$.

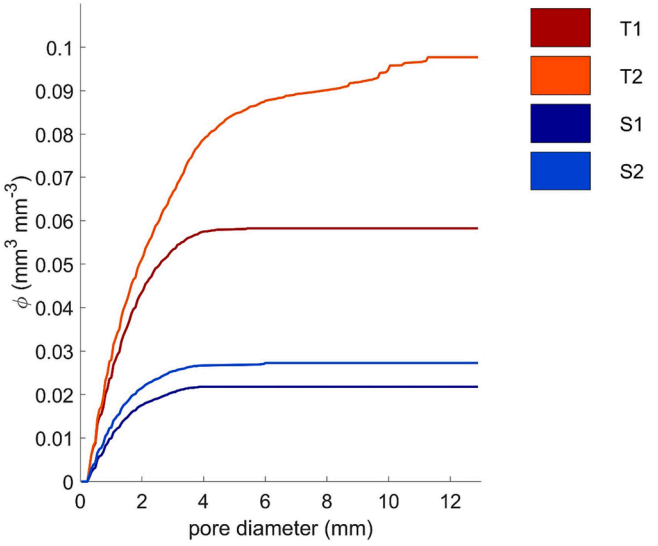

Fig. 5. Pore thickness distributions for the four samples shown as cumulative distribution functions of the porosity φ.

Fig. 6. Illustration of the 40 × 40 × 85 mm^3 volumes for visualization of activated regions. The visualization was carried out using Drishti 2.6.5 (Limaye, 2012).

geometries: a value of zero means a constant value of wetted macropore surface area, which could arise due to film flow whereas a value of one implies a proportionality between wetted surface area and water content (Jarvis et al., 2017a). Combining equations (11) and (13) yields

$$q_{\ddagger} = K_{s(mac)} \left(\frac{\theta_{\ddagger}}{\phi} \right)^{\alpha} \tag{14}$$

where

$$\alpha = 3 - 2\beta \tag{15}$$

and the macropore saturated hydraulic conductivity $K_{s(mac)}$ is given by Kozeny's equation

$$K_{s(mac)} = c \left(\frac{\phi^3}{\sigma^2} \right) \tag{16}$$

In the following, we equated $q_{\ddagger}$ with the applied irrigation rates, $s_{\ddagger}$ with s as defined in equation (9) and $\theta_{\ddagger}$ with the image-derived water-filled macropores θ_w. For the two topsoil samples, the required state variables were available for sufficient irrigation rates to estimate α from regression (equations (13) and (15)). We also plotted $q_{\ddagger}$ against $\theta\ r_h^2$ in order to experimentally derive c (equation (11)), which we then compared with the theoretical value (equation (12)).

3. Results

3.1. Characterization of the imaged pore networks

Fig. 4a shows that the two topsoil samples had larger imaged porosities (ca. 0.058 and 0.097 $mm^3\ mm^{-3}$) than the two subsoil samples (ca. 0.023 and 0.027 $mm^3\ mm^{-3}$). The imaged pore space in both subsoil samples was poorly connected, with connection probabilities smaller than 0.25 and no percolating pore space (Fig. 4b & c). In contrast, the macropore networks in the two topsoil samples were very well connected, with percolating fractions of more than 0.8. The connection probabilities (ca. 0.68 and 0.77, see Fig. 4b) are almost exactly equal to the square of the percolating fraction, which means that the pore space is dominated by the largest cluster and only this cluster percolates (Jarvis et al., 2017b). In other words, the macropore network in both topsoil samples can be characterized as a single "giant" cluster with a pore volume well above the percolation threshold. This is in line with percolation thresholds in the range 0.03 to 0.05 $mm^3\ mm^{-3}$, which have earlier been reported for tilled agricultural soils (Jarvis et al., 2017b; Koestel et al., 2018). Fig. 5 shows the pore thickness distribution of the

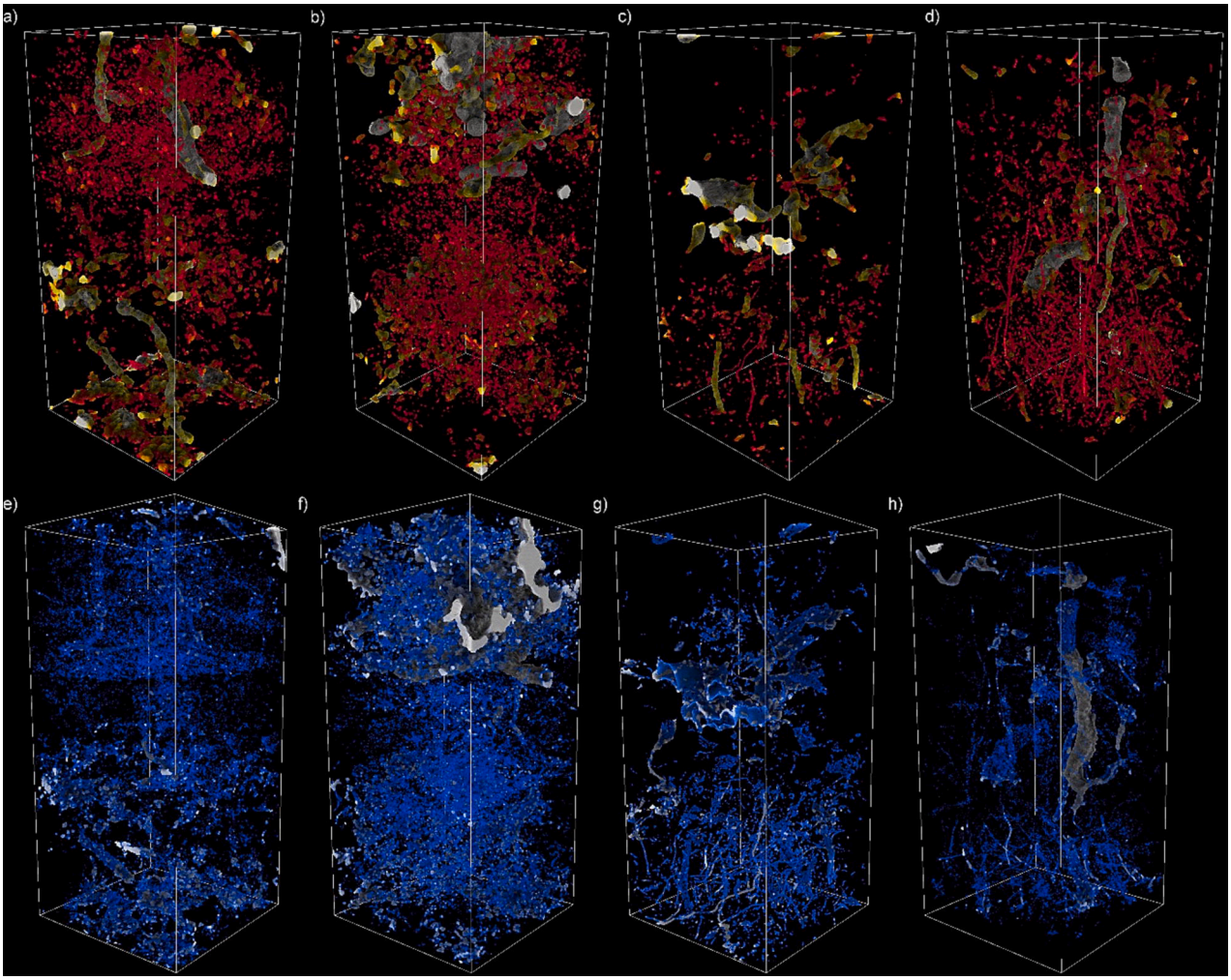

Fig. 7. Top row: 3-D depiction of the air-filled imaged macropores in all four soil samples under the maximal irrigation intensities (images A_i), i.e. (a) sample T1 at 50 mm h^{-1}, (b) sample T2 at 50 mm h^{-1}, (c) sample S1 at 5 mm h^{-1} and (d) sample S2 at 1 mm h^{-1} and the water-filled imaged macropores in all four soil samples under the maximal irrigation intensities (images W_i), i.e. (e) sample T1 at 50 mm h^{-1}, (f) sample T2 at 50 mm h^{-1}, (g) sample S1 at 5 mm h^{-1} and (h) sample S2 at 1 mm h^{-1}. 40 by 40 mm cutouts as illustrated in Fig. 6 are shown instead of the entire column to reveal the view on the pore structures in the center of each sample. The colors encode the local thickness of the activated regions where brighter colors mean larger local thicknesses of the depicted phases. The visualization was carried out using Drishti 2.6.5 (Limaye, 2012).

imaged pore networks. Except for sample T2, most of the imaged pore space in the samples had a diameter < 4 mm. In T2, about 10 % of the imaged pore space had a diameter of between 8 and 10 mm. These large macropores were located in the upper half of the sample.

3.2. Visualizations of air and water distributions

We used a region of interest with edge lengths of 40 mm in the X- and Y-directions (see Fig. 6) to illustrate qualitatively the distributions of air-filled imaged pores and detected water content increases. Fig. 7 shows the imaged air-filled voxels and voxels with detected water-content increases relative to the initial state under the largest investigated irrigation rates (i.e. 50 mm h^{-1} for the topsoil samples T1 and T2 and 5 mm h^{-1} and 1 mm h^{-1} for the subsoil samples S1 and S2, respectively). Note that samples T2 and S1 ponded under these irrigation rates, while T1 and S2 did not. In the topsoil samples (Fig. 7d and e), a restricting soil layer with a low air-filled macroporosity is visible at a depth of ca. 30 mm below the upper surface of the ROI and ca. 40 mm below the soil surface. This depth probably corresponds to the base of the seedbed. Fig. 7 also demonstrates that the imaged air-filled pore space as well as voxels with increases in water content were more sparsely distributed in the subsoil samples. In the subsoil, a larger fraction of the imaged air and water was contained in cylindrical structures with diameters of up to 0.5 mm. In contrast, the majority of the imaged air and water in the topsoil samples appeared to be located rather in pores between soil aggregates (or fragments) created during tillage operations (not shown). Large water-filled macropores were almost exclusively restricted to the upper half of the topsoil samples, the only exception was a large macropore in sample S2 (Fig. 7h).

An example (sample T2) of the gradual increase in detected water content and the concomitant decrease in imaged air-filled pores is shown in Fig. 8. This figure shows clearly that the largest macropores in T2 only filled when the column ponded under an irrigation intensity of 50 mm h^{-1}, while some of the imaged macropores remained air-filled even under ponding.

Fig. 8 also depicts evidence of capillary forces at work, illustrated by curved air–water interfaces and the gradual filling of the pore-network with water where narrower pore-throats were saturated first. Some of the smaller macropores remained air-filled even under larger irrigation rates for which neighboring pores with larger diameters had already filled up. Fig. 8 suggests the presence of water films along some of the imaged macropore surfaces. Note, however, that we cannot rule out that a part of the imaged water-film like features may have resulted from registration inaccuracies.

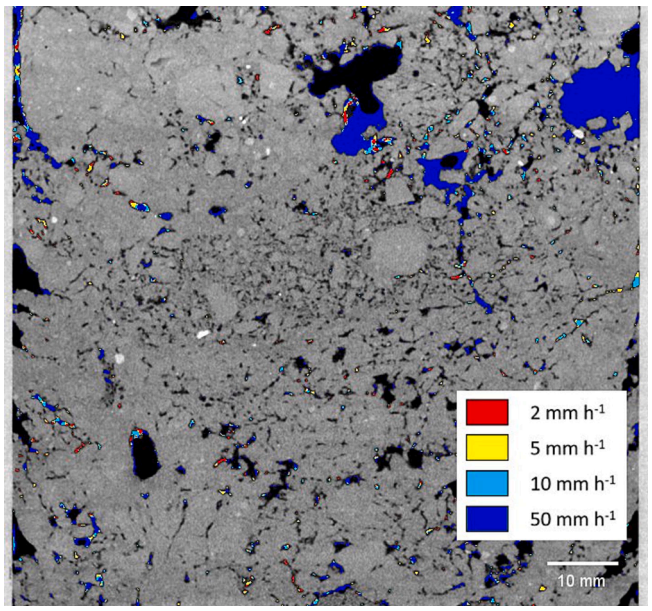

Fig. 8. Vertical cross-section approximately through the rotational axis of sample T2. The gray-scale shows the local X-ray attenuation, which is approximately linearly related to the material density. Black regions correspond to air-filled pores, gray regions to the soil matrix and white regions to sand grains and gravel. Activated voxels are colored according to the steady-state irrigation rate under which it was first activated. The calibrated X-ray gray values are shown for all non-activated voxels.

3.3. Air and water distributions: Quantitative observations

Fig. 9a & b show that water content increased monotonically in the topsoil samples as the irrigation rate increased, whilst the air content concomitantly decreased. There was an especially pronounced increase in water content at the final irrigation rate for sample T2, which corresponded to a drastic decrease in air-filled macroporosity (Fig. 9c). Otherwise, the increases in macropore saturation and the corresponding decreases in imaged air-filled macroporosity were gradual (Fig. 9a-c). Fig. 9d shows that except for column T2, the degree of water saturation in the imaged macropores was equal to or less than ca. 30 % even at the final irrigation rate.

Fig. 10 shows the thicknesses of the activated regions. Note that these are not identical to the water-filled pore-size distribution, since they also include water in corners or films and water in the imaged soil matrix.

Fig. 11 illustrates the connectivity of the air-filled pore space in the four columns at the varying water flow rates. Remember that the imaged pore networks in the subsoil samples did not percolate (Fig. 4c). Fig. 11c shows that 45 % of the imaged pore space in these two subsoil samples also had no connection to the soil surface. Under steady state irrigation, the entrapped air fraction increased to values larger than 0.7 (Fig. 11c), while the connection probability of the air phase decreased from ca. 0.2 prior to the irrigation to values of less or equal than 0.1 (Fig. 11a). In contrast, for all but the largest flow rate (50 mm h^{-1}), the air phase in the imaged macroporosity of the two topsoils columns was still highly connected, with percolating fractions of 70 to 80 % (i.e. values close to that of the imaged pore space itself, Fig. 4a). Fig. 11c illustrates that only ca. 18 to 25 % of the air in the imaged pore space in the two topsoil columns can be considered as entrapped (i.e. with no imaged air-filled connection to the soil surface) at water flow rates of up to 10 mm h^{-1}. The entrapped air fraction subsequently increased dramatically to ca. 50 to 100 % in the two topsoil columns at the largest water flow rate (50 mm h^{-1}; Fig. 11c). In sample T2, the air phase then no longer percolated (Fig. 11b) and this occurred concurrently with the establishment of a percolating water phase in the imaged macropores (Fig. 12d).

In contrast, the water phases in the imaged macropores at all flow rates in sample T1 and at all flow rates less than 50 mm h^{-1} in sample T2 did not percolate and small connection probabilities indicated a large number of individual disconnected clusters (Fig. 12b).

3.4. Macropore water content, wetted surface area, hydraulic radius and flow rate

Fig. 13a shows that the imaged wetted macropore surface area increased with both flow rate and the degree of imaged macropore saturation (Fig. 9d) although it never exceeded 75 % of the imaged macropore surfaces (Fig. 13b). The hydraulic radius was approximately constant for all samples and irrigation rates except at the highest flow rates for sample T2 (Fig. 13b), where it was clearly larger as a consequence of the saturation of several large macropores in the upper half of this sample (see Fig. 7f). The composite parameter c could be derived from equation (11) for the two topsoil samples T1 and T2 with large coefficients of determination of $R^2 = 0.95$ and 0.94, with values of 2,171 and 142 $mm^{-1}h^{-1}$, respectively (Fig. 14a). The goodness-of-fit was mostly determined by the data point for the largest irrigation rate. Somewhat better fits were obtained when the largest irrigation rate was omitted (Fig. 14b). More similar values for c were then found for both columns (1,255 and 848 $mm^{-1}h^{-1}$ for T1 and T2 respectively).

Fig. 14c confirms that the degree of saturation of the macropore network in the topsoils was related to the fractional wetted macropore surface area by a power law (see equation (13). Linear regressions using equation (13) on logged data yielded β values of 0.80 and 0.55 for the topsoil samples T1 and T2 (see Fig. 14c), corresponding to kinematic wave exponents α of 1.4 and 1.9 (see equation (15). If only the data from the first three irrigation rates (2, 5 and 10 mm h^{-1}), were taken into account, the goodness-of-fit improved (Fig. 14d) and yielded similar β values for both samples of 0.89 and 0.87 (kinematic exponents α of 1.22 and 1.26).

4. Discussion

4.1. Flow processes

Our study illustrates the complexity of water flow processes in soil in the near-saturated range. We did not observe a strictly sequential filling-up of pores with increasing diameter during the increasing irrigation rates (Fig. 10) as would be predicted by soil water flow models based on the concept of pore networks as capillary bundles. Instead, we found that increases in flow rate indeed led to the filling of larger pores, but often starting with corner flow (Fig. 8). We also found visual evidence of film flow (Fig. 8).

The water flowing through the macropore network in sample T2 at an irrigation rate of 50 mm h^{-1} was the only observed occasion in which the water in the imaged pores mostly comprised a single 'giant' (82 % of the total visible water, see Fig. 12d) percolating cluster, since the connection probability (=0.695) is almost equal to the square of the fraction of the water phase that percolates (=0.694; Jarvis et al., 2017b). It follows that for all flow processes in other samples and at other irrigation rates, flow bottlenecks smaller than the image resolution were important, which is also reflected in the absence of percolating water-phases. We did not expect such a result. As discussed above, tension-disc infiltrometer measurements at the sampling site (Jarvis and Messing, 1995; Messing and Jarvis, 1993) strongly suggest that the water flow should predominantly take place in pores with effective diameters larger than the image resolution (330 μm) at irrigation rates of 5 mm h^{-1} and larger. At the same time, the network of imaged macropores in the topsoil samples was well connected and percolating (Fig. 4b & c). We favor two possible explanations for the lack of observed connected water phases in the imaged macropores. On the one hand, the imaged network of air and water-filled pores is subject to residual illumination bias and image noise, which could have led to severed connections in the imaged

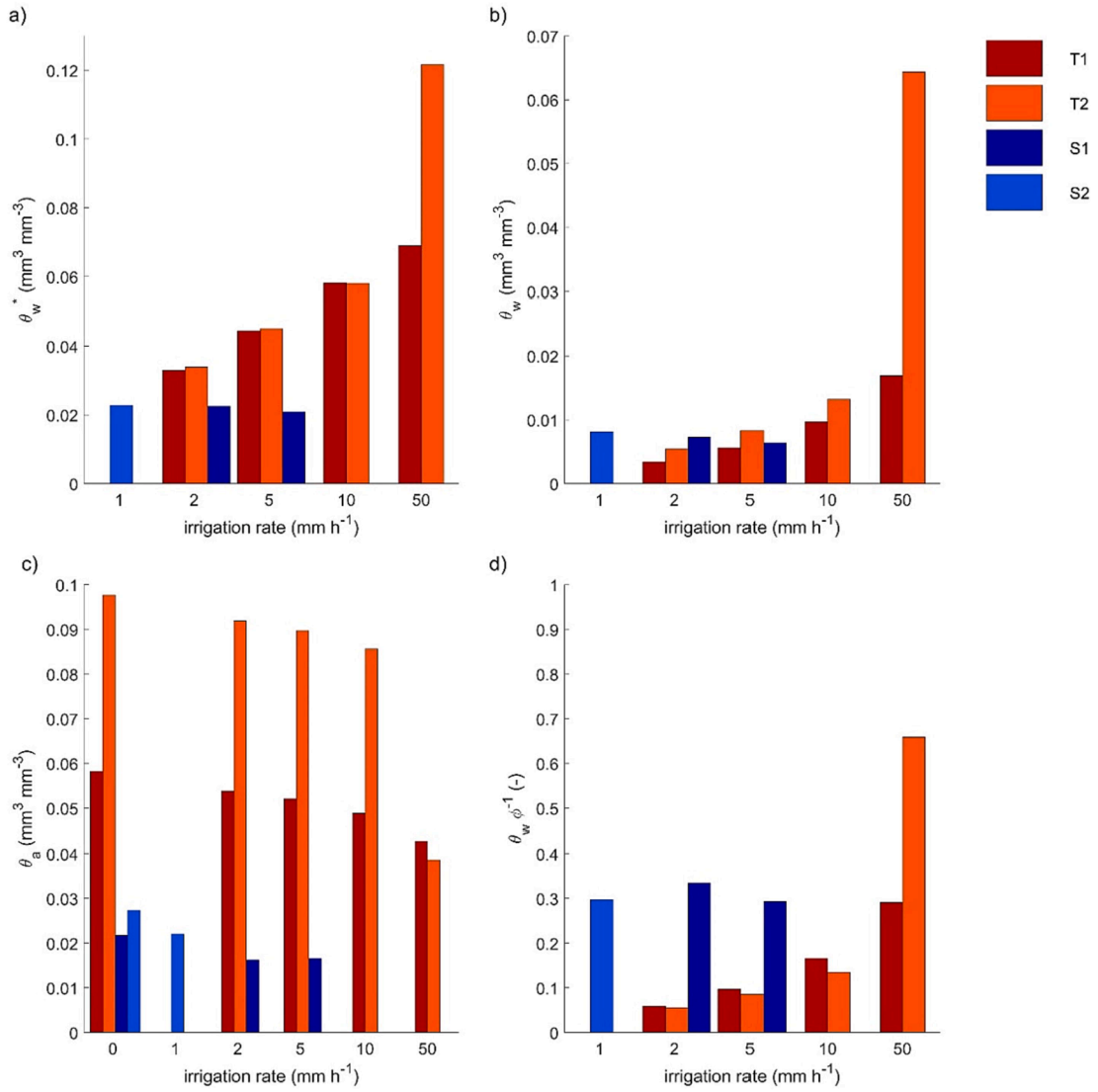

Fig. 9. (a) fraction of voxels with detected water content increase, θ_w*; (b) image resolvable macropores with detected water content increase, θ_w; (c) air content for image–resolved macropores, θ_a; (d) degree of water saturation of image-resolvable macropores, $\theta_w\ \varphi^{-1}$.

air and water phases. In this respect, it should be remembered that errors in imaging the pore network are directly transmitted to the water in X-ray visible pores (see equation (4)). On the other hand, the lack of connectivity of the water-filled imaged pores might also be caused by locally intermittent flow processes in the form of non-stationary rivulets, droplets or plugs or by flow in thin films with thicknesses smaller than the image resolution of approximately 330 μm. Both are known macropore flow mechanisms (e.g. Germann, 1987; Tofteng et al., 2002; Gjettermann et al., 2004; Ghezzehei and Or, 2005; Nimmo, 2021) and neither would be detected with the setup of our study.

4.2. Air entrapment

We found a considerable amount of entrapped air in the macropore system (Fig. 11c), which is known to occur during water flow in macropore networks close to saturation. As the soil wets up, the displaced air will either be vented through the soil surface or become entrapped and compressed by the infiltrating water (Carrick et al., 2011; Culligan et al., 2000; Dixon and Peterson, 1971; Dixon and Linden, 1972; Snehota et al., 2015). Fig. 8 illustrates the entrapment nicely, showing a large fraction of air-filled pore space remaining in sample T2 even under the largest irrigation rate, which led to ponding on this soil column.

The macropore networks in the topsoil columns exhibited large connection probabilities (Fig. 4b). As a consequence it is not surprising that the connection probabilities for the air phase in the topsoil samples fell almost exactly on a 1:1 line when plotted against the square of the fraction of the percolating air-filled pore space, (i.e. $[\theta_{a(p)}\ \varphi^{-1}]^2$ at water flow rates of 10 mm h^{-1} or less. This is illustrated in Fig. 15. It indicates that one cluster of the imaged air phase is much larger than any other cluster and that this cluster is percolating (Jarvis et al., 2017b), and that consequently, this air can be vented. The drop in connectivity of the air-phase in the macropores for both topsoil columns under the largest irrigation rate is striking (Fig. 11a & b). It corresponds to the separation of this single air-filled pore cluster into smaller disconnected parts. Fig. 15 depicts, however, that a dominating, percolating air-cluster still existed in sample T1 at the highest irrigation rate of 50 mm h^{-1}. The hydraulic conductivity of this sample was large enough to prevent ponding. Hence, the fraction of entrapped air also remained moderate. The other investigated topsoil sample T2 ponded at 50 mm h^{-1}. This was probably caused by a flow-restricting layer near the center of sample T2 (Fig. 7f), which resulted in a "build-up" of water above this layer and led to a large amount of entrapped air (Fig. 11), especially in the lower half of this soil sample (Fig. 8). The subsoil samples ponded at much lower flow rates. The large fraction of air remaining in the imaged pore space

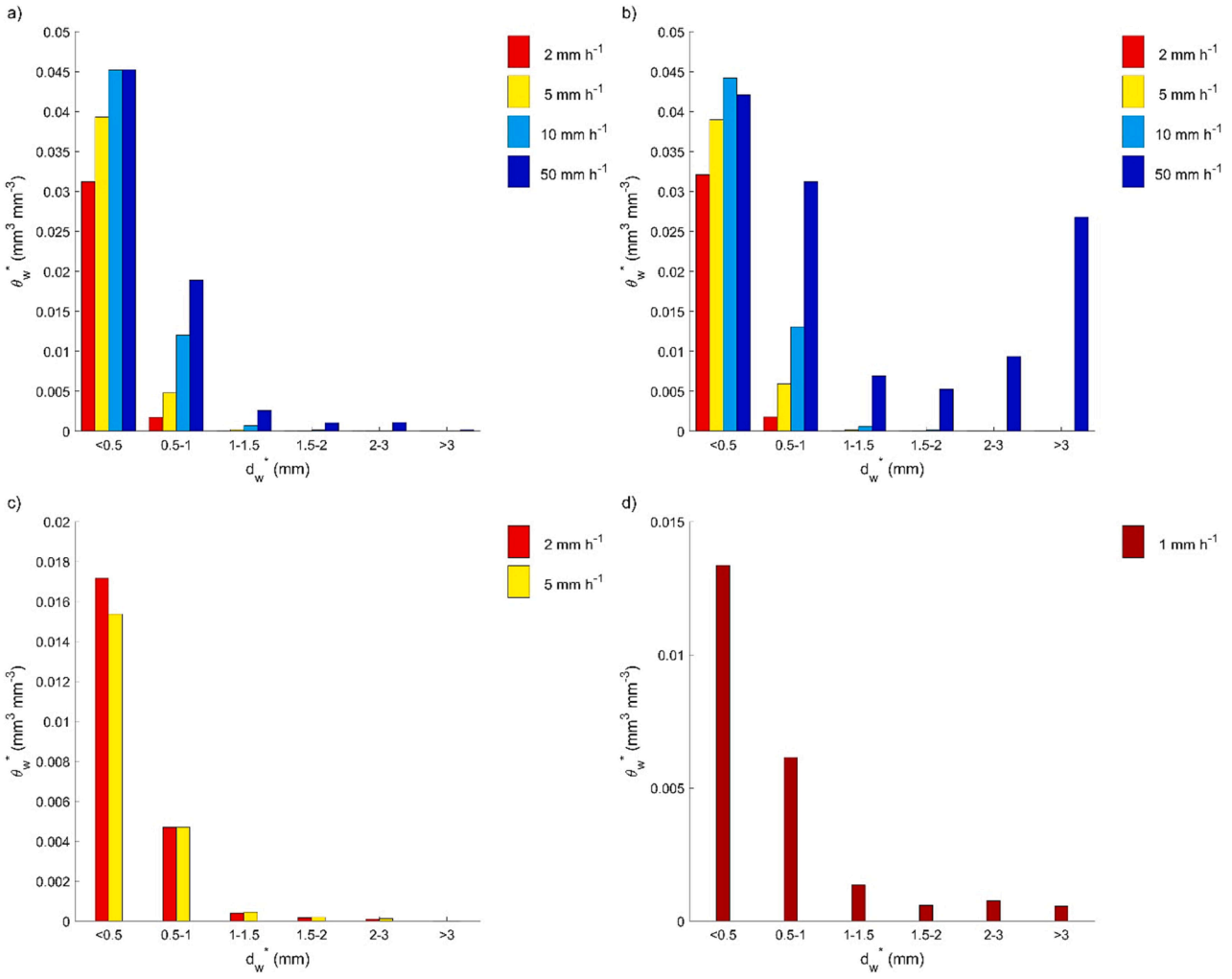

Fig. 10. Image detected changes in volume fraction of activated voxels θ_w* under varying steady-state irrigation rates grouped by average local diameters d_w* for samples (a) T1, (b) T2, (c) S1 and (d) S2.

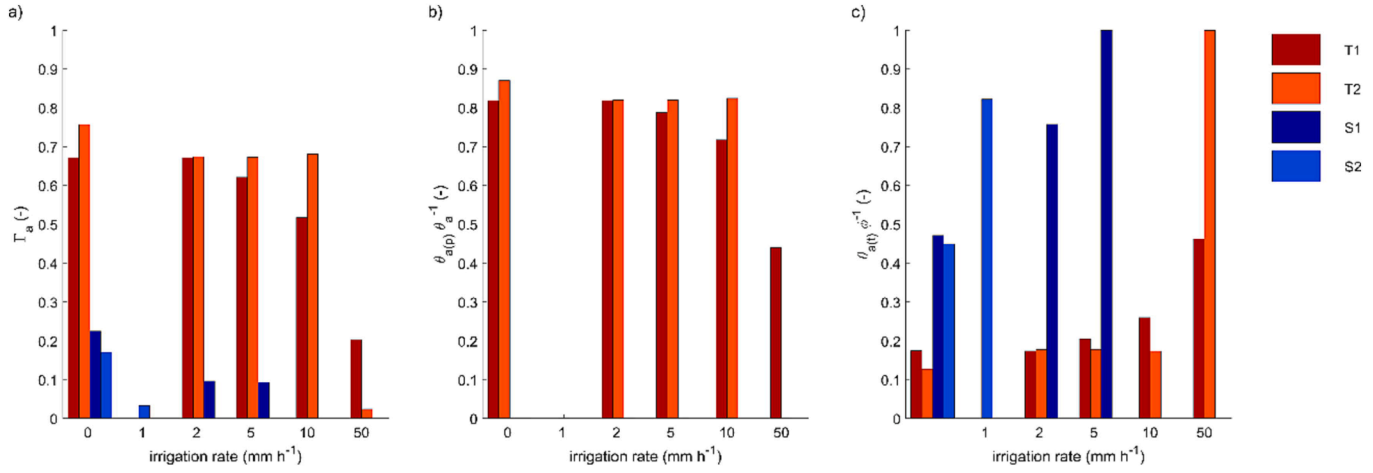

Fig. 11. Connectivity of the imaged air phase (a) connection probability Γ_a (b) the percolating air fraction and (c) the fraction of entrapped air, i.e. the imaged air-filled pores without connection to the topmost surface of the considered ROI. Note that the fraction of entrapped air was set to 1 when ponding was observed.

of these two samples is probably a consequence of its disconnected nature (Fig. 7), which is quantified by their relatively low connection probability (Fig. 4).

4.3. Test of the Kozeny equation

All fitted values for *c* underestimated the theoretical value of 7 million by more than three orders of magnitude. This large discrepancy

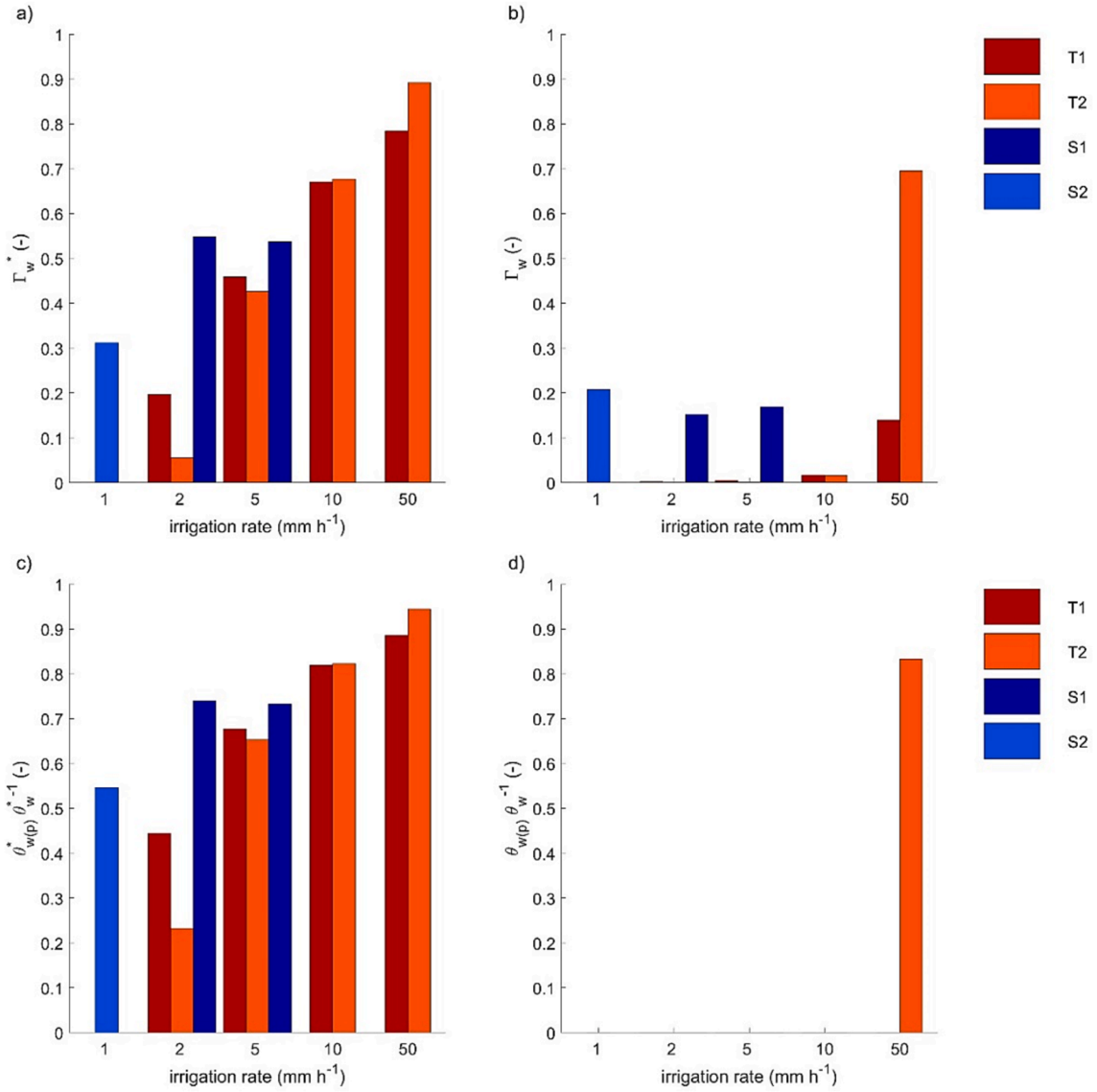

Fig. 12. Connectivity metrics for the water phase (a) connection probability Γ_w for voxels with detected water content changes, (b) connection probability Γ_w for the water phase in imaged macropores, (c) fraction of percolating water phase for voxels with detected water content changes and (d) fraction of percolating water phase in imaged macropores.

indicates that one or more of the assumptions underlying Stokes law generalized at the macroscopic scale (equation (11)) were not met. The assumption that is most obviously violated is that the water flows through an equivalent channel or non-interacting pathways of negligible variation in thickness, i.e. an absence of bottlenecks. It has long been known that the Kozeny equation (equation (16)) is not appropriate to describe the saturated hydraulic conductivity of natural soils as they are characterized by a very wide range of pore sizes (e.g. Childs, 1969; Hoffmann-Riem et al., 1999). Clearly, the presence of flow bottlenecks means that the theory breaks down even for the more restricted range of pore diameters found in macropore networks (Fig. 5; see also Jarvis, 2008). Furthermore, not all the imaged water-filled pore volumes will have contributed to water flow, due to the presence of dead-end pores with only slow water movement or no flow at all. Our X-ray images (see Fig. 7) indicate the complex nature of the flow networks in these soil columns with multiple inter-connected pathways and a relatively wide range of pore diameters, bottlenecks and dead-end pores. Air was also entrapped in the poorly connected networks in the subsoil and at high water input rates in the topsoil samples. Flow rates through such networks will be much smaller than suggested by equations (11), (12) and (16). Indeed, the saturated hydraulic conductivity calculated by equation (16) will be highly sensitive to ϕ, the conducting macroporosity, as it is raised to the power three. Various proposals have been made to modify Kozeny's equation to account for the effects of connectivity and pore size distribution on permeability (e.g. Berg, 2014).

4.4. Relationship between macropore saturation and wetted surface area

Macropore water saturation and wetted macropore surface area showed a log–log linear relationship as required by the theory underlying the kinematic wave equation (Jarvis et al., 2017a), but only if the largest irrigation rate was omitted. In this case, values for the kinematic exponent α of 1.22 and 1.26 were found, indicating predominant flow in corners and rivulets (Fig. 3), which is in line with observations and inferences made in this study, including the fact that the hydraulic radius remained approximately constant with irrigation rate. Intuitively, one might expect that β asymptotically approaches zero (and α approaches 3) at water contents near saturation, as more and more rivulets and water-films establish until all macropore surfaces are wetted and water contents can only be increased by filling-up wetted pores (see Fig. 3).

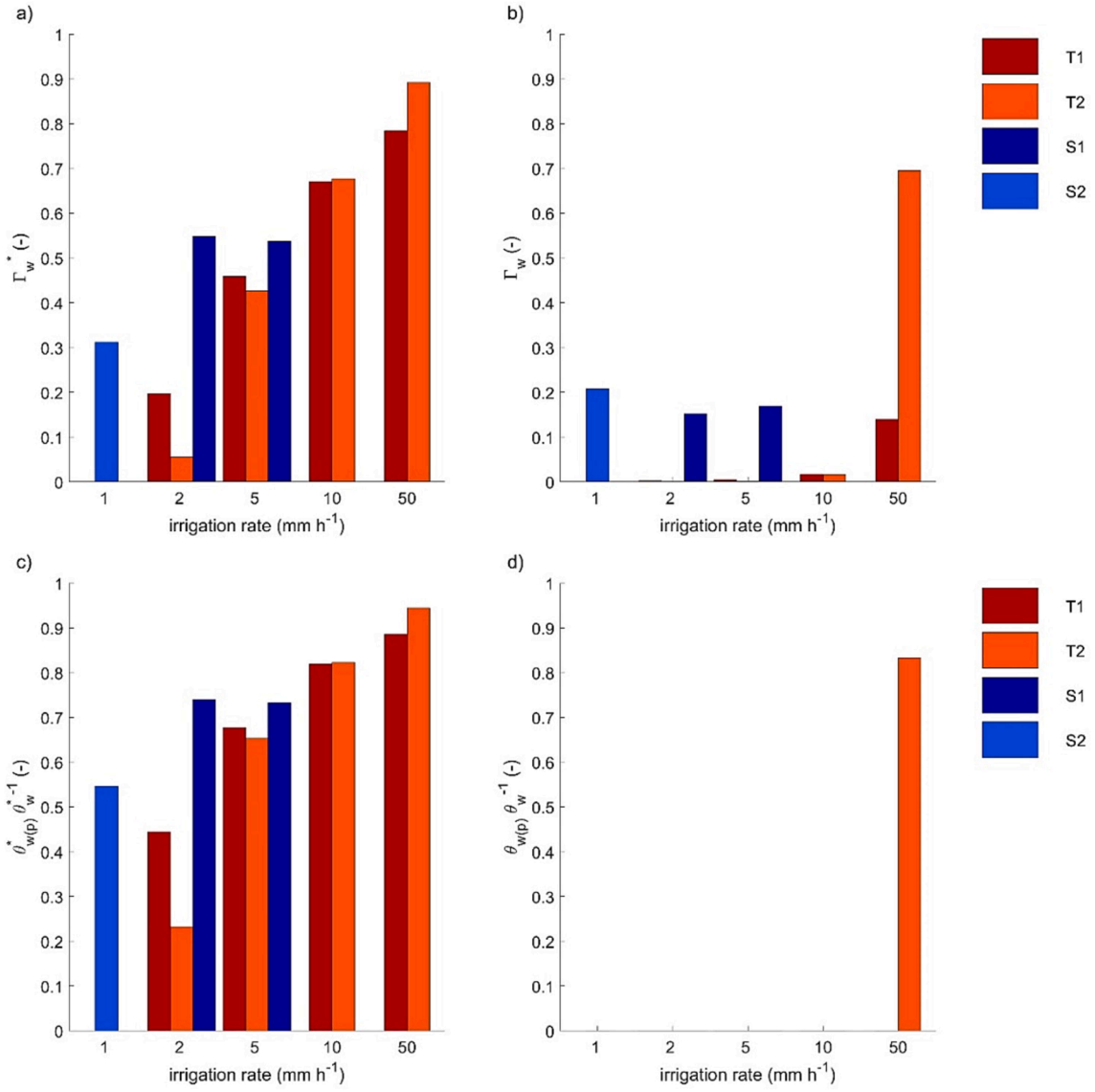

Fig. 13. (a) specific wetted surface areas of image-resolvable macropores s; (b) fractional specific wetted surface area of image-resolvable macropores s σ^{-1}; (c) hydraulic radius r_h.

The larger coefficients of determination and smaller kinematic exponents found when disregarding the largest irrigation intensities support this intuition.

4.5. Saturated hydraulic conductivity of the macropore network

Based on the experimentally fitted *c* values (equation (11)), saturated hydraulic conductivities of the macropore system $K_{s(m)}$ of 576 and 96 mm h^{-1} were calculated using equation (16) for samples T1 and T2 respectively, if the data from all the irrigation rates were included. If the largest irrigation rate was excluded, $K_{s(m)}$ values of 270 and 468 mm h^{-1} were obtained for T1 and T2 respectively. The estimated $K_{s(m)}$ values derived from fitting equation (14) were similar (252 and 112 mm h^{-1} for T1 and 88 and 117 mm h^{-1} for T2 if the largest irrigation rate was not considered). While it is not possible to judge the accuracy of the $K_{s(m)}$ estimation for sample T1, it is obvious that $K_{s(m)}$ calculated for T2 overestimated the true saturated hydraulic conductivity irrespective of which equation or data was used. It must have been between 10 and 50 mm h^{-1} since the sample started to pond at the larger irrigation rate. Such an overestimation of $K_{s(m)}$ may also be explained by the important role of flow bottlenecks in controlling the saturated hydraulic conductivity (Koestel et al., 2018; Schlüter et al., 2020).

5. Conclusions

X-ray imaging proved to be a valuable tool for illustrating near-saturated water flow processes. We found that a significant fraction of the macropore network remained air-filled during the irrigation experiments, but that this air phase only became entrapped when the irrigation rate was very close to the saturated hydraulic conductivity of the samples. We found a lack of connectivity of the water-phase in the imaged macropores, even though the macropore networks themselves were dense and highly connected in the topsoil samples. We attributed this to flow in thin films below image resolution and/or intermittent flow, although further reductions in image noise and heterogeneous image illumination would be needed to allow unequivocal identification of these flow mechanisms. A reduction in the sample size would help in this respect, not only by improving image resolution, but also by providing a better signal-to-noise ratio and more homogeneous illumination. We therefore suggest focusing future experiments on smaller sample sizes until the X-ray imaging hardware has improved sufficiently to allow for high-resolution imaging of larger samples, which would be

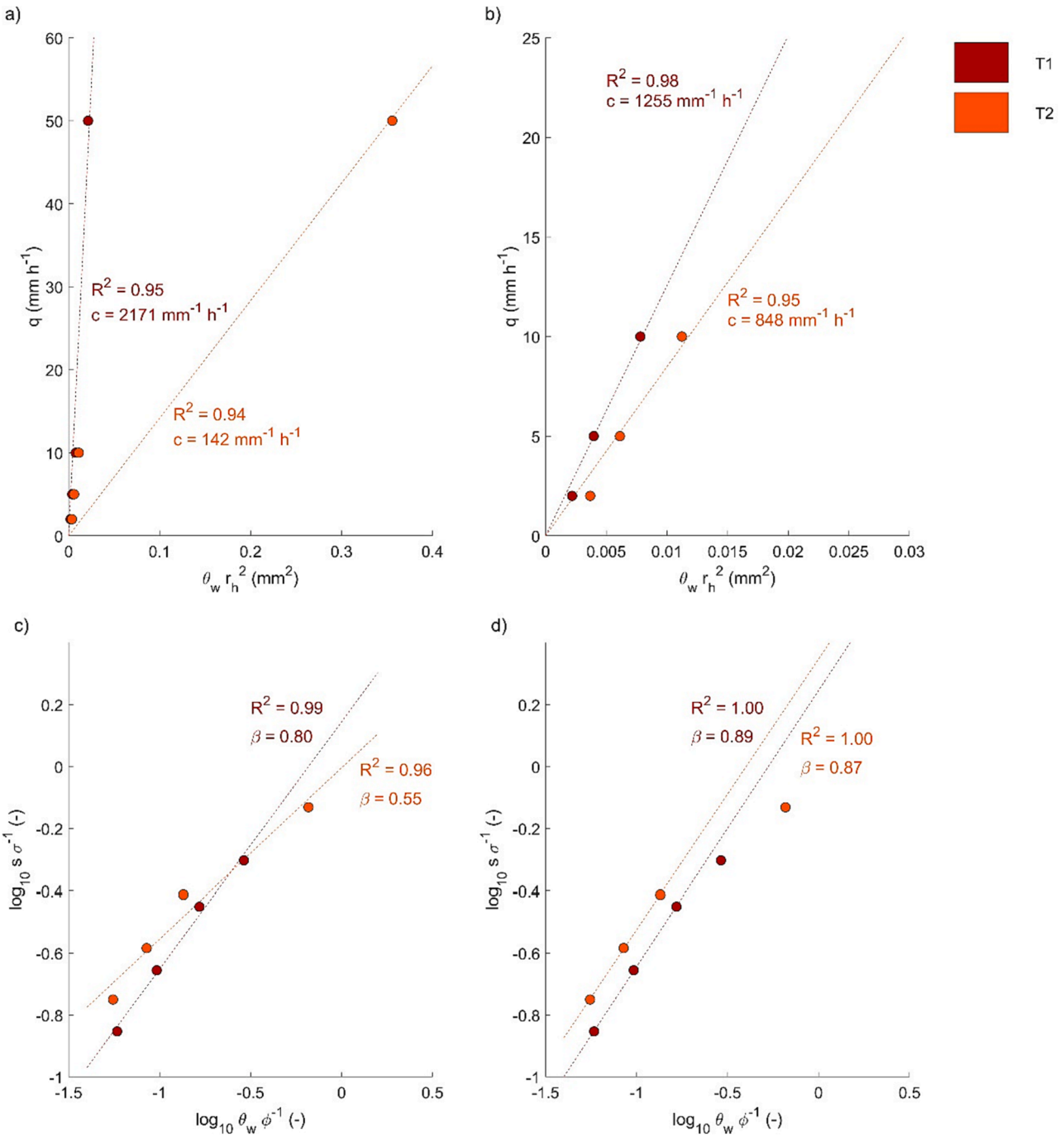

Fig. 14. (a) irrigation rate q plotted against the water content in the imaged macropores multiplied the square of the hydraulic radius r_h; factor c was obtained by resolving equation (11) by minimizing least squares in the Euclidean domain; the data is shown in the logarithmic domain for illustration purposes; (b) like a) but only taking the first three irrigation rates into account when fitting c; (c) the logarithm of the wetted surface area fraction s σ^{-1} versus the logarithm of the water saturation of the imaged macropores $\theta_w \varphi^{-1}$; the exponent β is shown, too, including the goodness of fit (see equation (13); (d) like c) but only taking the first three irrigation rates into account when fitting β.

more representative for the macropore networks encountered in the field (Koestel et al., 2020).

Despite the technical difficulties, we found that the kinematic wave model could be parameterized from the image data following the approach proposed in Jarvis et al., (2017a). However, we also demonstrated that the saturated hydraulic conductivity of the macropores would be dramatically overestimated if the underlying theory from Stokes and Kozeny were strictly followed, most likely because it fails to account for flow bottlenecks, dangling pores and air entrapment in the macropore networks. Of course, in practical applications of the kinematic wave equation, the saturated macropore hydraulic conductivity can be measured and does not need to be estimated from the (inappropriate) theory. Past experience suggests that the kinematic wave equation usually works well when used as a semi-empirical model in this way (Demand and Weiler, 2021; Hincapié and Germann, 2009; Larsbo et al., 2005).

Follow-up experiments are required in the future to evaluate if the X-ray derived image kinematic wave parameters match with parameterizations obtained from classical drainage experiments. We suggest that imaging of the air–water distributions in the soil should be combined

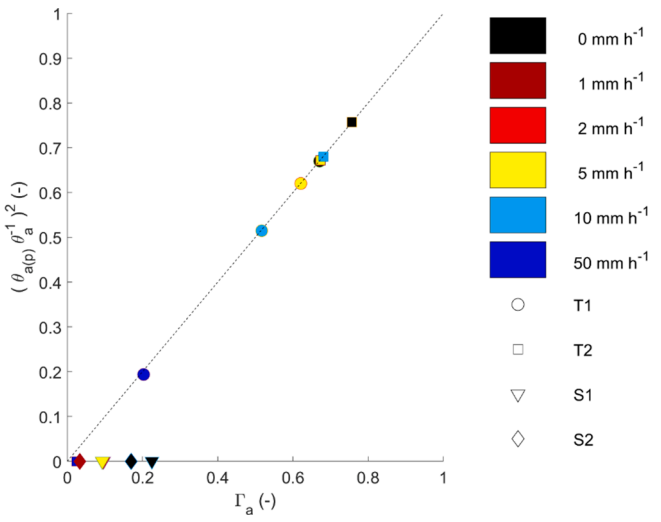

Fig. 15. The connection probability of the air phase, Γ_a plotted against the square of the fraction of the percolating air phase.

with the use of an X-ray sensitive tracer, since a reasonable match between kinematic wave parameters derived by X-ray imaging and drainage experiments most likely requires separate identification of the backbone network and the dead-end pores. In the future, this kind of study could be paired with 3-D numerical simulation modeling at the pore scale to obtain estimates of macropore flow model parameters from X-ray images of macropore networks.

Declaration of competing interest

The authors declare that they have no known competing financial interests or personal relationships that could have appeared to influence the work reported in this paper.

Data availability

Data will be made available on request.

Acknowledgements

This study was financed by FORMAS research grant 2016-00922, 'Quantifying macropore flow by X-ray tomography to improve model predictions of contaminant leaching in soil'.

Appendix A

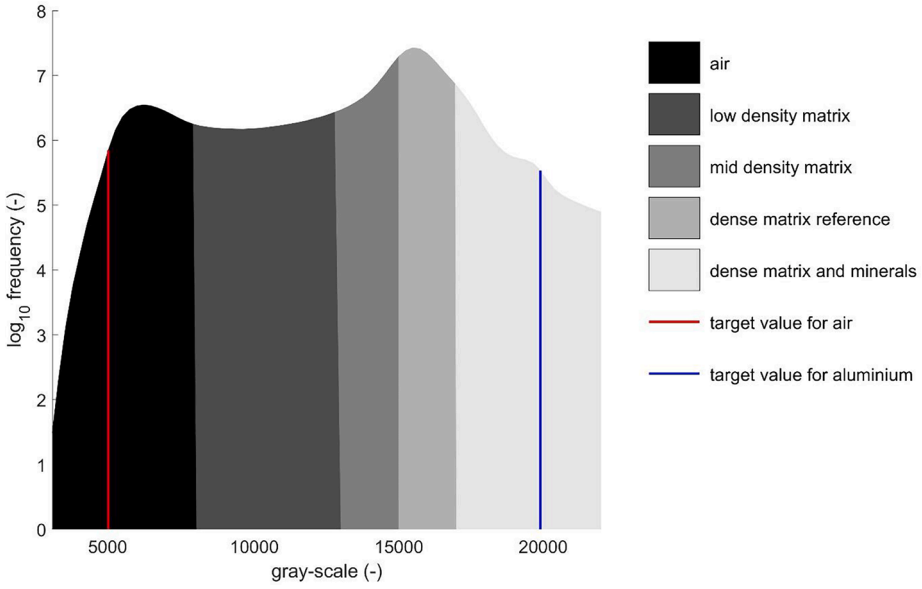

Fig. A1. Histogram of the image of column T2 prior to the irrigation and after the standard SoilJ gray-scale calibration. The dense matrix phase between gray-values of 15,000 and 17,000 was chosen as a reference gray-value for the extended gray-scale calibration. Also indicated is the gray-scale range of low density matrix-voxels, which could become activated voxels (gray-values between 8,000 and 13,000).

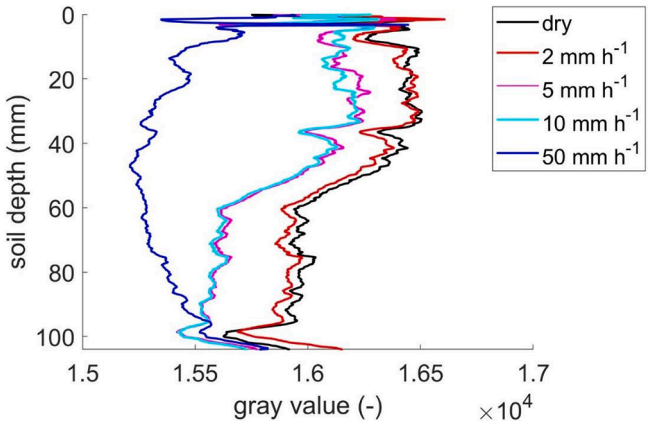

Fig. A2. Example for vertical fluctuations of the gray values in the dense matrix phase ($\gamma_{dmp,z}$) with irrigation rate for sample T2 before the extended gray-scale calibration step.

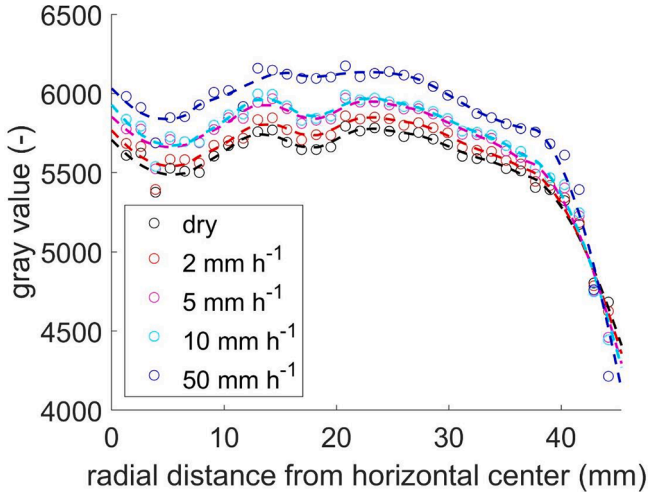

Fig. A3. Example for radial fluctuations of the gray values of the air-phase ($\gamma'_{air,r}$) with irrigation rate for sample T2 after correcting for vertical gray-scale fluctuations but before correcting of the radial fluctuations in the extended gray-scale calibration step.

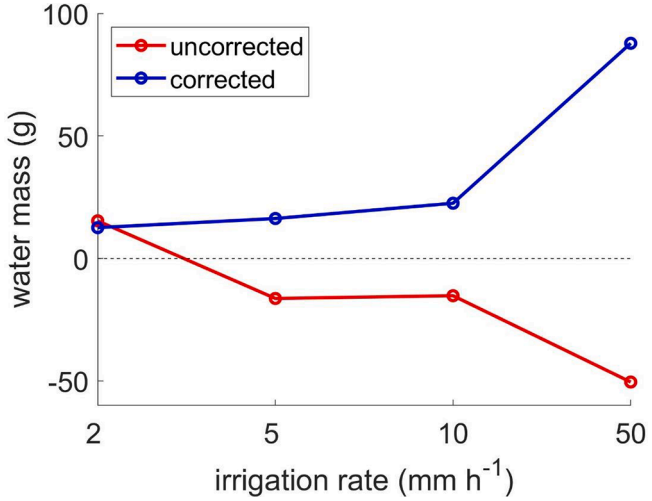

Fig. A4. Exemplary illustration of X-ray derived water masses in sample T2 before (uncorrected) and after (corrected) the extended gray-scale calibration step.

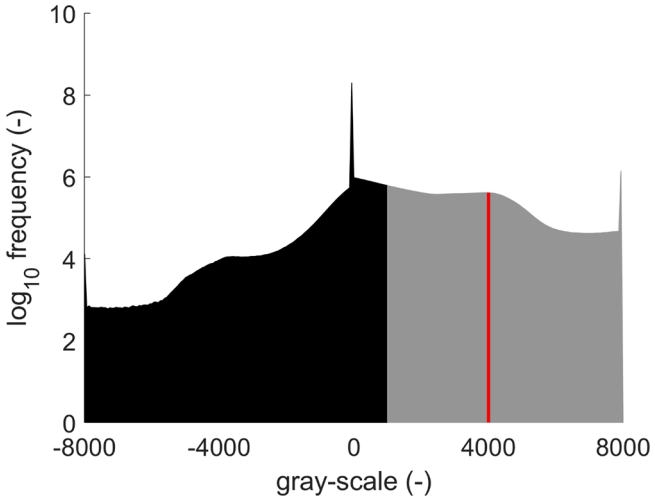

Fig. A5. Histogram of difference image of column T2 between at 50 mm h^{-1} irrigation intensity for illustration of the gray-scale range of activated voxels. The gray-scale range for which voxels were not considered as activated is shown in black, the one for which voxels were considered activated in gray. The red line marks the gray-value of 4000 which we identified to correspond approximately to water-filled pores.

References

Arah, J.R.M., Ball, B.C., 1994. A functional model of soil porosity used to interpret measurements of gas-diffusion. Eur. J. Soil Sci. 45 (2), 135–144.

Berg, C.F., 2014. Permeability description by characteristic length, tortuosity, constriction and porosity. Transp. Porous Media 103 (3), 381–400.

Beven, K., Germann, P., 1982. Macropores and water flow in soils. Water Resour. Res. 18 (5), 1311–1325.

Carrick, S., Buchan, G., Almond, P., Smith, N., 2011. Atypical early-time infiltration into a structured soil near field capacity: The dynamic interplay between sorptivity, hydrophobicity, and air encapsulation. Geoderma 160 (3–4), 579–589.

Childs, E.C., 1969. An Introduction to the Physical Basis of Soil Water Phenomena. Wiley-Interscience, London xiii + 493.

Culligan, P.J., Barry, D.A., Parlange, J.Y., Steenhuis, T.S., Haverkamp, R., 2000. Infiltration with controlled air escape. Water Resour. Res. 36 (3), 781–785.

Dal Ferro, N., Strozzi, A.G., Duwig, C., Delmas, P., Charrier, P., Morari, F., 2015. Application of smoothed particle hydrodynamics (SPH) and pore morphologic model to predict saturated water conductivity from X-ray CT imaging in a silty loam Cambisol. Geoderma 255–256, 27–34.

Demand, D., Selker, J.S., Weiler, M., 2019. Influences of macropores on infiltration into seasonally frozen soil. Vadose Zone J. 18 (1), 2–14.

Demand, D., Weiler, M., 2021. Potential of a gravity-driven film flow model to predict infiltration in a catchment for diverse soil and land cover combinations. Water Resour. Res. 57 (5).

Dixon, R.M., Linden, D.R., 1972. Soil air pressure and water infiltration under border irrigation. Soil Sci. Soc. Am. J. 36 (6), 948–953.

Dixon, R.M., Peterson, A.E., 1971. Water infiltration control - Channel system concept. Soil Sci. Soc. Am. Proc. 35 (6), 968.

Gackiewicz, B., Lamorski, K., Kochiieru, M., Sławiński, C., Hsu, S.Y., Chang, L.C., 2022. Hybrid modelling of saturated water flow in percolating and non-percolating macroporous soil media. Geoderma 406.

Gao, M., Li, H.Y., Liu, D., Tang, J., Chen, X., Chen, X., Blöschl, G., Ruby Leung, L., 2018. Identifying the dominant controls on macropore flow velocity in soils: A meta-analysis. J. Hydrol. 567, 590–604.

Germann, P.F., 1985. Kinematic wave approach to infiltration and drainage into soil macropores. Trans. ASAE 28 (3), 745–749.

Germann, P.F., 1987. The three modes of water flow through a vertical pipe. Soil Sci. 144 (2), 153–154.

Ghezzehei, T.A., Or, D., 2005. Liquid fragmentation and intermittent flow regimes in unsaturated fractured media. Water Resour. Res. 41 (12), 1–10.

Gjettermann, B., Hansen, H.C.B., Jensen, H.E., Hansen, S., 2004. Transport of phosphate through artificial macropores during film and pulse flow. J. Environ. Qual. 33 (6), 2263–2271.

Heijs, A.W.J., Delange, J., Schoute, J.F.T., Bouma, J., 1995. Computed-tomography as a tool for nondestructive analysis of flow patterns in macroporous clay soils. Geoderma 64 (3–4), 183–196.

Helliwell, J.R., Sturrock, C.J., Grayling, K.M., Tracy, S.R., Flavel, R.J., Young, I.M., Whalley, W.R., Mooney, S.J., 2013. Applications of X-ray computed tomography for examining biophysical interactions and structural development in soil systems: a review. Eur. J. Soil Sci. 64 (3), 279–297.

Hincapié, I., Germann, P.F., 2009. Impact of initial and boundary conditions on preferential flow. J. Contam. Hydrol. 104 (1–4), 67–73.

Hoffmann-Riem, H., van Genuchten, M., Flühler, H., 1999. General model for the hydraulic conductivity of unsaturated soil. In: van Genuchten, M., Leij, F., Wu, L. (Eds.), Characterization and Measurement of the Hydraulic Properties of Unsaturated Porous Media. Univ. California, Riverside, pp. 31–42.

Hunt, A., Ewing, R., Ghanbarian, B., 2014. Percolation theory for flow in porous media. Lecture Notes in Physics. Springer, Heidelberg (Germany).

Jarvis, N.J., 2007. A review of non-equilibrium water flow and solute transport in soil macropores: Principles, controlling factors and consequences for water quality. Eur. J. Soil Sci. 58 (3), 523–546.

Jarvis, N., Koestel, J., Larsbo, M., 2017a. Reply to 'Comment on "Understanding preferential flow in the vadose zone: Recent advances and future prospects" by N. Jarvis et al.'. Vadose Zone J. 16(5).

Jarvis, N., Koestel, J., Larsbo, M., 2016. Understanding preferential flow in the vadose zone: Recent advances and future prospects. Vadose Zone J. 15 (12).

Jarvis, N., Larsbo, M., 2012. MACRO (v5.2): model use, calibration, and validation. Trans. ASABE 55 (4), 1413–1423.

Jarvis, N., Larsbo, M., Koestel, J., 2017b. Connectivity and percolation of structural pore networks in a cultivated silt loam soil quantified by X-ray tomography. Geoderma 287, 71–79.

Jarvis, N.J., Messing, I., 1995. Near-saturated hydraulic conductivity in soils of contrasting texture measured by tension infiltrometers. Soil Sci. Soc. Am. J. 59 (1), 27–34.

Katuwal, S., Norgaard, T., Moldrup, P., Lamandé, M., Wildenschild, D., de Jonge, L.W., 2015. Linking air and water transport in intact soils to macropore characteristics inferred from X-ray computed tomography. Geoderma 237–238, 9–20.

Klein, S., Staring, M., Murphy, K., Viergever, A., Pluim, P.W.J., 2010. Elastix: A toolbox for intensity-based medical image registration. IEEE Trans. Med. Imaging 29, 196–205.

Koestel, J., 2018. SoilJ: An ImageJ plugin for the semiautomatic processing of three-dimensional X-ray images of soils. Vadose Zone J. 17 (1).

Koestel, J., Dathe, A., Skaggs, T.H., Klakegg, O., Ahmad, M.A., Babko, M., Giménez, D., Farkas, C., Nemes, A., Jarvis, N., 2018. Estimating the permeability of naturally structured soil from percolation theory and pore space characteristics imaged by X-Ray. Water Resour. Res. 54 (11), 9255–9263.

Koestel, J., Larsbo, M., 2014. Imaging and quantification of preferential solute transport in soil macropores. Water Resour. Res. 50 (5), 4357–4378.

Koestel, J., Larsbo, M., Jarvis, N., 2020. Scale and REV analyses for porosity and pore connectivity measures in undisturbed soil. Geoderma 366, 114206.

Lamandé, M., Schjønning, P., Dal Ferro, N., Morari, F., 2021. Soil pore system evaluated from gas measurements and CT images: A conceptual study using artificial, natural and 3D-printed soil cores. Eur. J. Soil Sci. 72 (2), 769–781.

Larsbo, M., Roulier, S., Stenemo, F., Kasteel, R., Jarvis, N., 2005. An improved dual-permeability model of water flow and solute transport in the vadose zone. Vadose Zone J. 4 (2), 398–406.

Larsbo, M., Koestel, J., Jarvis, N., 2014. Relations between macropore network characteristics and the degree of preferential solute transport. Hydrol. Earth Syst. Sci. 18 (12), 5255–5269.

Legland, D., Arganda-Carreras, I., Andrey, P., 2016. MorphoLibJ: integrated library and plugins for mathematical morphology with ImageJ. Bioinformatics 32 (22), 3532–3534.

Limaye, A., 2012. Drishti: a volume exploration and presentation tool. In: S.R. Stock (Ed.), Developments in X-Ray Tomography VIII.

Lissy, A.S., Sammartino, S., Ruy, S., 2020. Can structure data obtained from CT images substitute for parameters of a preferential flow model? Geoderma 380.

Löv, Å., Sjöstedt, C., Larsbo, M., Persson, I., Gustafsson, J.P., Cornelis, G., Kleja, D.B., 2017. Solubility and transport of Cr(III) in a historically contaminated soil –

Evidence of a rapidly reacting dimeric Cr(III) organic matter complex. Chemosphere 189, 709–716.
Luo, L., Lin, H., Li, S., 2010. Quantification of 3-D soil macropore networks in different soil types and land uses using computed tomography. J. Hydrol. 393 (1–2), 53–64.
Messing, I., Jarvis, N.J., 1993. Temporal variation in the hydraulic conductivity of a tilled clay soil as measured by tension infiltrometers. J. Soil Sci. 44 (1), 11–24.
Mooney, S.J., 2002. Three-dimensional visualization and quantification of soil macroporosity and water flow patterns using computed tomography. Soil Use Manag. 18 (2), 142–151.
Nimmo, J.R., 2021. The processes of preferential flow in the unsaturated zone. Soil Sci. Soc. Am. J. 85 (1), 1–27.
Perret, J., Prasher, S.O., Kantzas, A., Langford, C., 1999. Three-dimensional quantification of macropore networks in undisturbed soil cores. Soil Sci. Soc. Am. J. 63 (6), 1530–1543.
Pierret, A., Capowiez, Y., Belzunces, L., Moran, C.J., 2002. 3D reconstruction and quantification of macropores using X-ray computed tomography and image analysis. Geoderma 106(3-4), 247-271.Renard, P., Allard, D., 2013. Connectivity metrics for subsurface flow and transport. Advances in Water Resources 51(0), 168-196.
Sammartino, S., Michel, E., Capowiez, Y., 2012. A novel method to visualize and characterize preferential flow in undisturbed soil cores by using multislice helical CT. Vadose Zone J. 11 (1).
Sammartino, S., Lissy, A.-S., Bogner, C., Van Den Bogaert, R., Capowiez, Y., Ruy, S., Cornu, S., 2015. Identifying the functional macropore network related to preferential flow in structured soils. Vadose Zone J. 14 (10).
Scheibe, T.D., Perkins, W.A., Richmond, M.C., McKinley, M.I., Romero-Gomez, P.D.J., Oostrom, M., Wietsma, T.W., Serkowski, J.A., Zachara, J.M., 2015. Pore-scale and multiscale numerical simulation of flow and transport in a laboratory-scale column. Water Resour. Res. 51 (2), 1023–1035.
Schindelin, J., Arganda-Carreras, I., Frise, E., Kaynig, V., Longair, M., Pietzsch, T., Preibisch, S., Rueden, C., Saalfeld, S., Schmid, B., Tinevez, J.-Y., White, D.J., Hartenstein, V., Eliceiri, K., Tomancak, P., Cardona, A., 2012. Fiji: an open-source platform for biological-image analysis. Nat. Methods 9 (7), 676–682.
Schlüter, S., Albrecht, L., Schwärzel, K., Kreiselmeier, J., 2020. Long-term effects of conventional tillage and no-tillage on saturated and near-saturated hydraulic conductivity – Can their prediction be improved by pore metrics obtained with X-ray CT? Geoderma 361.
Schlüter, S., Sheppard, A., Brown, K., Wildenschild, D., 2014. Image processing of multiphase images obtained via X- ray microtomography: A review. Water Resour. Res. 50 (4), 3615–3639.
Schneider, C.A., Rasband, W.S., Eliceiri, K.W., 2012. NIH Image to ImageJ: 25 years of image analysis. Nat. Methods 9 (7), 671–675.
Shamonin, D., Bron, E., Lelieveldt, B., Smits, M., Klein, S., Staring, M., 2014. Fast parallel image registration on CPU and GPU for diagnostic classification of Alzheimer's disease. Front. Neuroinf. 7 (50).
Snehota, M., Jelinkova, V., Sobotkova, M., Sacha, J., Vontobel, P., Hovind, J., 2015. Water and entrapped air redistribution in heterogeneous sand sample: Quantitative neutron imaging of the process. Water Resour. Res. 51 (2), 1359–1371.
Soto-Gómez, D., Vázquez Juíz, L., Pérez-Rodríguez, P., López-Periago, J.E., Paradelo, M., Koestel, J., 2020. Percolation theory applied to soil tomography. Geoderma 357, 113959.
Tofteng, C., Hansen, S., Jensen, H.E., 2002. Film and pulse flow in artificial macropores. Hydrol. Res. 33 (4), 263–274.